ABSTRACT

Title of Document: VIRUS ENABLED 3D NANO-ARRAY ELECTRODES FOR INTEGRATED LI/NA-ION MICROBATTERIES

Yihang Liu, Master of Science, 2013

Directed By: Professor, Chunsheng Wang, Chemical and Biomolecular Engineering

Multilayers of functional materials (carbon/electrode/nickel) were hierarchically architectured over tobacco mosaic virus (TMV) templates that were genetically modified to self-assemble in a vertical manner on current-collectors for battery applications. The spaces formed between individual rods effectively accommodated the volume expansion and contraction of electrodes during charge/discharge, while surface carbon coating engineered over these nanorods further enhance the electronic conductivity. The microbattery based on self aligned nanoforests with precise arrangement of various auxiliary material layers including a central nanometric metal core as direct electronic pathway to current collector, can deliver high energy density and stable cycling stability. C/$LiFePO_4$/Ni/TMV nanoforest cathodes for Li-ion batteries and C/Sn/Ni/TMV nanoforest anodes for Na-ion batteries were assembled using physical sputtering deposition. Both 3D nanoforest electrodes show exceptional cycling stability and rate capability.

VIRUS ENABLED 3D NANO-ARRAY ELECTRODES FOR INTERGRATED LI/NA-ION MICROBATTERIES

By

Yihang Liu

Thesis submitted to the Faculty of the Graduate School of the
University of Maryland, College Park, in partial fulfillment
of the requirements for the degree of
[Master of Science]
[2013]

Advisory Committee:
Professor Chunsheng Wang, Chair
Professor Nam Sun Wang
Professor Dongxia Liu

Dedication

To my parents:

Thank you for your unconditional love and support. Thank you for your unwavering faith and absolute belief in my abilities.

Acknowledgements

First and foremost, I would like to express my deep and sincere gratitude to my supervisor, Dr. Chunsheng Wang. I am really honored to work under his guidance.

I would like to thank Dr. Nam Sun Wang and Dr. Dongxia Liu for serving on my committee and taking time attending my defense.

I would like to thank Dr. Junchen Guo, Dr. Yanting Luo, Dr. Yujie Zhu, Dr. Yunhua Xu and Dr. Xilin Chen, for mentoring me during my research years in the group.

I would like to acknowledge all the other members in Dr. Chunsheng Wang's group members, with whom I have worked, and because of whom my graduate experience has been one that I will cherish forever.

Table of Contents

Dedication ii
Acknowledgements iii
Table of Contents iv
List of Figures vi
Chapter 1: Introduction 1
1.1 Background 1
1.2 Lithium-ion battery system 2
1.3 Microbatteries 5
1.3.1 Background of microbatteries 5
1.4 Challenges of microbatteries 7
1.4.1 Cracking during heat-treatment 8
1.4.2 Low conductivity of cathode materials 8
1.4.3 Volume change of cathode and anode materials 8
1.5 Current techniques to enhance the microbattery electrodes 9
1.5.1 Annealing strategies and substrate modification 9
1.5.2 Co-deposition with conductive material 10
1.5.3 Nanoarchitectured 3D microbattery electrodes 10
1.6 Objective of this research 13
Chapter 2. Virus Enabled 3D Current Collector 15
2.1 Introduction 15
2.2 Experimental 16
Chapter 3: Architecturing Hierarchical Function Layers on Self-Assembled Viral Templates as 3D Nano-Array Electrodes for Integrated Li-ion Microbatteries 18
3.1 Introduction 18
3.2 3D C/$LiFePO_4$/Ti/Ni/TMV1cys nanoforest cathode preparation 23
3.3 Characterization of the 3D $LiFePO_4$ nanoforest cathode 25
3.3.1 SEM 26
3.3.2 XRD 29
3.3.3 TEM and EDS mapping profile 31
3.3.4 Raman spectra 33
3.4 Electrochemical tests result and discussion 34
3.4.1 Rate capability 35
3.4.2 Electrochemical impedance spectroscopy (EIS) 38
3.4.3 Cycling stability 41
3.5 Summary 44
Chapter 4: Tin Coated Virus Nanoforests for Sodium-Ion Battery Anodes 45
4.1 Introduction 45
4.2 3D C/Sn/Ni/TMV1cys nanoforest anode preparation 48
4.3 Characterization of 3D C/Sn/Ni/TMV1cys nanoforest anode 49
4.3.1 SEM, TEM and EDS line scan profile 50
4.3.2 Raman spectra 52
4.4 Electrochemical tests result and discussion 53
4.4.1 Cyclic voltammetry 54
4.4.2 Cycling stability 56

4.4.3 After cycling SEM and TEM 58
4.5 Summary 60
Chapter 5: Conclusion and future work 61
5.1 Conclusion 61
5.2 Future work 62
Bibliography 64
Publication and Presentation 73
Publication 73
Publications that have appeared in print 73
Publications that have been submitted and are under review 74
Presentation 74
Presentations that have been delivered 74

List of Figures

Figure 1.1 Schematic structure of a typical lithium-ion battery and its discharge process.

Figure 1.2 The cross-section SEM image of $LiMn_2O_4$ thin film electrode prepared by radio-frequency sputtering deposition.

Figure 1.3 The cross-section SEM image of silicon electrode prepared by "Down Down" photolithography method.

Figure 1.4 The SEM image of $LiCoO_2$ nanorods prepared by "Bottom Up" template method.

Figure 2.1 The two main steps in the preparation of the virus enabled 3D current collector: TMV1cys self-assembling and nickel chemical deposition.

Figure 3.1 Schematic description of TMV-templated near-vertical assembly of $LiFePO_4$ nanoforest on current collector with multi-layered nano-hierarchical arrangement of active materials and electron conducting pathway.

Figure 3.2 The SEM images of the (a) Ti/Ni/TMV1cys on stainless steel, (b) as-deposited $LiFePO_4$/Ti/Ni/TMV1cys, (c) annealed $LiFePO_4$/Ti/Ni nanowire at 500^oC for 2 hours, (d) annealed $LiFePO_4$/Ti/Ni nanowire after 450 charge/discharge cycles at 1C rate, (e) carbon coated annealed $LiFePO_4$/Ti/Ni nanowire, (f) carbon coated annealed $LiFePO_4$/Ti/Ni nanowire after 450 charge/discharge cycles at 1C rate.

Figure 3.3 The XRD patterns of (a) as-deposited $LiFePO_4$nanwire forest, (b) annealed at 500^oC for 1 hour in vacuum, (c) annealed at 500^oC for 2 hours in vacuum. All the peaks in Figure S1 are indexed based on the XRD data base file (JCPDS-832092).

Figure 3.4 (a) TEM image of $LiFePO_4$/Ti/Ni nanowireafter annealing at 500^oC for 2 hours, (b) the high-resolution TEM image of the $LiFePO_4$ crystal. The EDS mapping profiles in the red mapping rectangle marked in (a) for Ni (c), Ti (d), P (e), and Fe (f). Li-ion diffusion channel (b axis direction) is marked in (b). (g) TEM image of $LiFePO_4$/Ti/Ni nanowire after 450 cycles at 1C rate. TEM image of C/$LiFePO_4$/Ti/Ni nanowire (h) before charge/discharge cycle, (i) enlarge figure of (h), (j) after 450 charge/discharge cycles at 1C rate.

Figure 3.5 Raman spectrum of the carbon coated $LiFePO_4$/Ti/Ni nanowire forest cathodes.

Figure 3.6 (a) The potential profiles of C/$LiFePO_4$/Ti/Ni, $LiFePO_4$/Ti/Ni nanowire forest cathodes, and $LiFePO_4$/Ti thin film cathode 0.1C charge/discharge current, and (b) rate performance of 3D C/$LiFePO_4$/Ti/Ni, 3D $LiFePO_4$/Ti/Ni nanowire forest cathodes, and 2D $LiFePO_4$/Ti thin film cathode at different charge/discharge currents.

Figure 3.7 Typical Nyquist plots of three $LiFePO_4$ cathodes (a) after 50 charge/discharge cycles at 1C rate and (b) after 450 charge/discharge cycles at 1C rate, obtained after charging the $LiFePO_4$ cathode to 3.6 V and relaxation for 2 hours.

Figure 3.8 The cycling stability and Coulombic efficiency of $LiFePO_4$ cathodes at 1C charge/discharge current.

Figure 4.1 Schematic illustrations of the 3D C/Sn/Ni/TMV1cys anode arrays and the cross-section of hierarchical structure of a single Sn nanorod.

Figure 4.2 SEM images of (a, b) as-deposited 3D Sn/Ni/TMV1cys and 3D C/Sn/Ni/TMV1cys anodes. TEM images of (c) a single C/Sn/Ni/TMV1cys nanorod, and its the EDS line scan mapping profile (d), (e) high-resolution TEM image of the

Sn crystal and the amorphous outer-layer, and (f) enlarged high-resolution TEM image of the Sn crystal of the red rectangle area in (e).

Figure 4.3 Raman spectra of 3D C/Sn/Ni/TMV1cys nanoforest anode.

Figure 4.4 Cyclic voltammetry of C/Sn/Ni/TMV1cys nanoforest anode with a scan rate of 0.1 mV s^{-1} between 0.0 and 2.0 V.

Figure 4.5 (a) Cycling performance of 2D Sn thin film, 3D Sn/Ni/TMV1cys, and 3D C/Sn/Ni/TMV1cys anodes, and sodiation/de-sodiation voltage profiles of (b) 2D Sn thin film, (c) 3D Sn/Ni/TMV1cys, and (d) 3D C/Sn/Ni/TMV1cys nanoforest anodes, at current density of 50 mA g^{-1}.

Figure 4.6 SEM images of (a) 3D Sn/Ni/TMV1cys anode and (b) 3D C/Sn/Ni/TMV1cys anode after 150 charge/discharge cycles at current density of 50mA g^{-1}. (c) TEM image of a single C/Sn/Ni/TMV1cys nanorod after 150 charge/discharge cycles at current density of 50mA g^{-1}, (d) enlarged high-resolution TEM image of the after-cycling amorphous Sn.

Chapter 1: Introduction

1.1 Background

Due to the increasing demand for fossil fuels and the environmental consequences of their use, more and more attention is being devoted to alternative energy sources for both energy generation and storage. Secondary battery systems have been considered as one of the energy storage strategy for the energy generated by renewable such as solar, wind and geothermal energy. Among the different types of batteries available in the marketplace, lithium-ion batteries have become the predominant battery technology for portable electronics, medical devices and electric vehicles.[1]

Lithium-ion batteries have three to four times the energy of standard lead-acid or nickel metal hydride batteries for the same size and weight, and can operate over a wide temperature range, typically from -20^{o}C to +50^{o}C and can last for hundreds or even thousands of charge/discharge cycles with near 100% energy efficiency and no memory effect. The high cell voltage (~3.5V) of lithium-ion batteries allows a single-cell-pack design for most portable devices.[1]

Due to the increase in the use of micro- and nano-electro-mechanical systems (MEMS/NEMS), there is greater demand for lithium-ion microbatteries as the power source. However, the low energy density and the poor stability of current traditional two dimensional thin film microbatteries greatly limits its applications. Thus, the main objective of this research is to develop new technologies to enhance the electrochemical performance of microbatteries.

1.2 Lithium-ion battery system

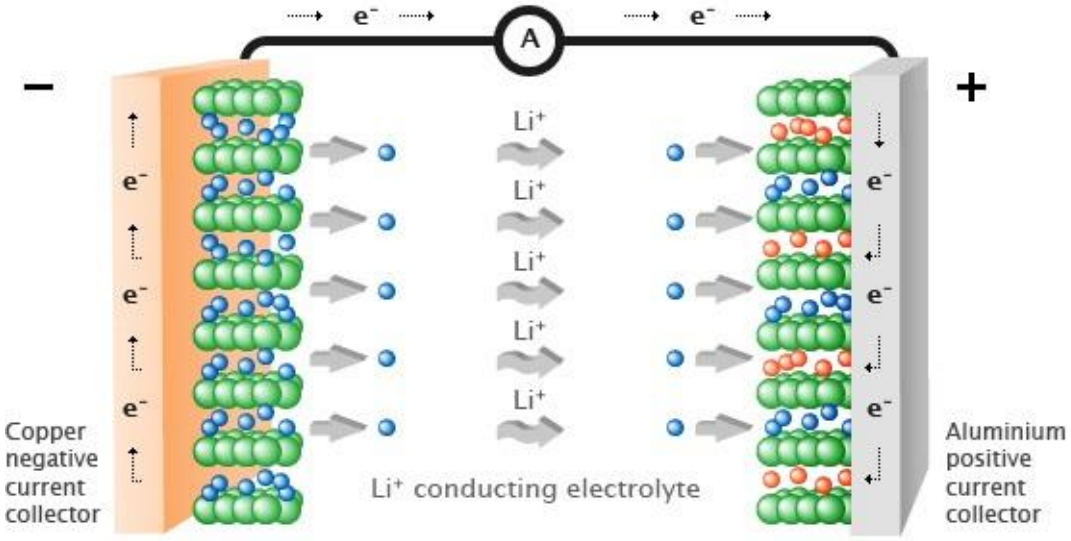

Figure 1.1 Schematic structure of a typical lithium-ion battery and its discharge process.[2] Copyright 2013 Nexeon LLC.

The three primary functional components of a lithium-ion battery are negative electrode, positive electrode and electrolyte. Insertion materials have been used as electrodes for many rechargeable lithium-ion battery systems. Electro-insertion can be referred to a redox reaction, where charge transfer occurs during the insertion of lithium ions into a solid host material. In lithium-ion batteries, lithium ions are usually stored in the positive electrode. The electrolyte allows the diffusion of ions, but is electronically insulating. The electrons are transferred through an external circuit to provide electricity. In order to keep natural, the positive electrode material compensates charge for the removal of lithium ion by oxidizing the transition metal present in the crystal lattice. Upon reaching the negative electrode, the lithium ions

intercalate into the material and recombine with the electrons, resulting in the reduction of the negative electrode material.[3]

During discharge in a lithium ion cell, the process is reversed as illustrated in Figure 1.1. Lithium ions transfer from the negative electrode material, through the liquid electrolyte, back to the positive electrode material while electrons shuttle from the negative electrode material to the positive electrode material through the external circuit. The lithium ions insert into the lattice of the positive electrode material and re-combine with the electrons. The electrode compensates charge via reducing the transition metal ion to its original oxidation state. In summary for a $LiCoO_2$/graphite cell:

Positive electrode (charging): $LiCoO_2 \rightarrow Li_{1-x}CoO_2 + xLi^+ + xe^-$

Negative electrode (charging): $xC_6 + xLi^+ + xe^- \rightarrow xLiC_6$

Positive electrode (discharging): $Li_{1-x}CoO_2 + xLi^+ + xe^- \rightarrow LiCoO_2$

Negative electrode (discharging): $xLiC_6 \rightarrow xC_6 + xLi^+ + xe^-$

Since lithium ions are transferred back and forth between the insertion materials present in positive and negative electrodes, as lithium ions flow through the electrolyte, the electrons flow through the external circuit, powering the portable device and electric vehicle. Thus, the electrode materials in the battery system must allow for the conductivity of both lithium ions and electrons. The rate capability of lithium-ion batteries mainly depends on the dimensional stability of the host material during insertion and extraction of lithium ion and on the kinetics of the lithium ion and electron transport in the host material. Mechanical stresses occur during lithiation and de-lithiation processes, causing cracks in the materials, which can eventually lead

to collapse. This lack of structural integrity reduces, and in some cases can be fatal to the electronic conductivity of the battery system, thus limiting the cycle life of the cell. Nevertheless, electrode materials exist that are stable during lithium insertion and removal processes. These low strain materials have volume changes less than 10% between the fully lithiated and delithiated states.

Graphite has been the predominant anode material for lithium-ion batteries since the launch of the first commercial lithium-ion battery. During the past decade, much effort has been directed toward identifying alternative anode materials that have higher theoretical capacity, higher charge/discharge rate and greater electrode stability. Insertion alloys (Si, Sn, Ge), redox metal oxides, and carbon allotropes have been considered as anode materials for the next-generation lithium-ion batteries.[1]

Unlike the anode, for which high-storage capacity materials are known to exist, the comparatively low storage capacity of most known cathode materials has been recognized as a major limiting factor in the overall performance of lithium-ion batteries. Since the successful introduction of the $LiCoO_2$ cathode in 1991,[4] other positive electrodes that have been investigated for commercial applications fall mainly into two categories.[5] The first group is layered compounds with a close packed oxygen negative ions lattice, in which transition metal positive ions present in layers between the negative ions and lithium ions are inserted into the available layers. The materials belong to this group gain the advantages of higher working voltage and specific energy density than the second group due to their highly oxidizing redox-active couples and compact lattices. These materials are compositional variations of layered $LiCoO_2$, such as $LiNiO_2$, $LiMnO_2$ and $LiNi_{1-x}Co_xO_2$, as well as spinel

structures derived from $LiMn_2O_4$.[6] The second group consists of metal oxides such as V_2O_5 and MnO_2, and transition metal phosphates, such as the olivine type $LiFePO_4$. Although their operating voltage is slightly lower than the materials in the first group, the less cost, enhanced safety and better kinetics of these compounds make them competitive cathode candidates.[7]

1.3 Microbatteries

1.3.1 Background of microbatteries

There is a growing interest in the micro- and nano-electro-mechanical systems (MEMS/NEMS) which are small, portable and flexible for applications that range from entertainment to retail automation to military devices. These products may be displays, medical devices, sensors or a variety of other kinds of devices and the dimension of the devices might be as small as micrometers or even nanometers. Because of the tiny size of the device, traditional casting techniques are not suitable for the electrode preparation.[8]

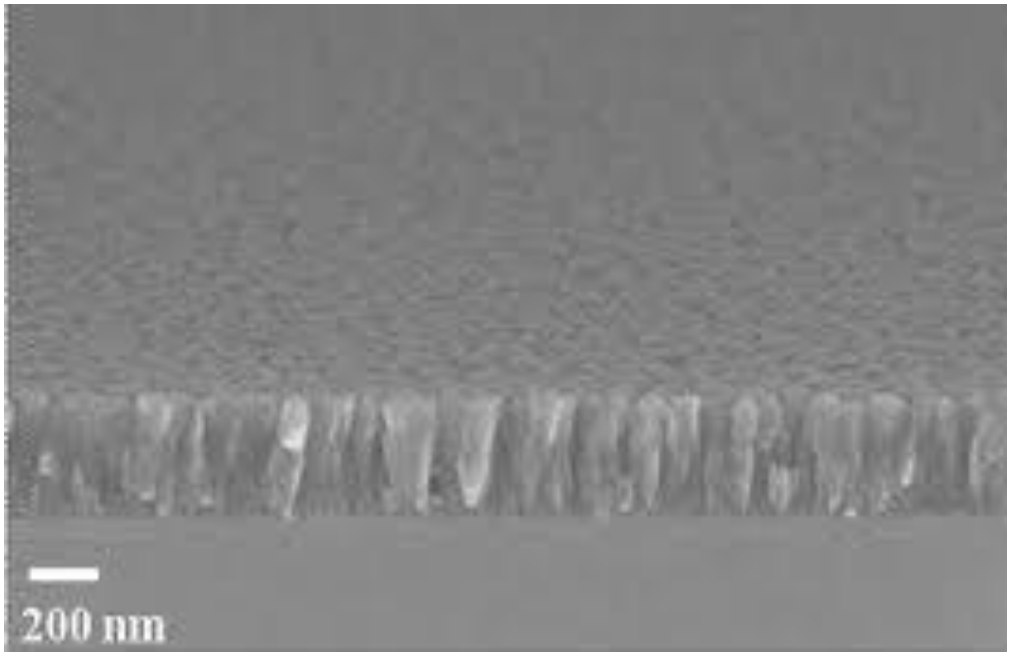

Figure 1.2 The cross-section SEM image of $LiMn_2O_4$ thin film electrode prepared by radio-frequency sputtering deposition.[12] Copyright 2007 Elsevier B. V.

In order to control the loading mass and the morphology of the electrodes of the micro-battery precisely, deposition techniques such as radio-frequency magnetron sputtering, plasma laser deposition and physical vapor deposition are widely used in the fabrication of traditional 2D thin film microbatteries, as shown in Figure 1.2.[9] Thin film micro-batteries are built layer by layer, which is similar to an ordinary lithium-ion battery structure, but much thinner. The thickness of the deposited 2D thin film may vary from hundreds of nanometers to tens of micrometers. The active materials used for the cathodes and anodes of micro-batteries are familiar compounds for ordinary lithium-ion batteries as discussed above, but the nanostructures and the cycling performance of the thin film electrodes may be quite different from those of typical battery electrodes formed from powders. The thin film electrodes are dense

and homogeneous without added material such as carbon black, binders or electrolytes. When deposited at room temperatures, the films of cathodes, such as $LiCoO_2$, V_2O_5, $LiMn_2O_4$, $LiFePO_4$ are amorphous or nanocrystalline.[10-13] Crystallizing the cathode film generally improves the lithium chemical diffusivity in the cathode material, and hence the power delivered by the battery, by 1-2 orders of magnitude.

For the microbattery anode, some designs use a vapor-deposited metallic lithium film as the anode. With a mechanically and chemically stable solid electrolyte such as LiPON, the lithium metal anodes give excellent charge-discharge cycling life at high charge/discharge current without any lithium dendrites. The chief drawback of metallic lithium anodes is the limited fabrication temperature, less than 180^oC, which prevents melting of the lithium metal.[14] In recent years, materials such as Sn and Si, which have been considered as the anode for the next-generation lithium-ion batteries, have been fabricated into thin film electrode to obtain a higher capacity and energy density.

1.4 Challenges of microbatteries

Although significant effort has been made to advance microbatteries, before reaching commercialization, many challenges remain. The major challenges of traditional 2D thin film microbatteries involve the cracks during heat-treatment in the fabrication process, the intrinsic insulating property of cathode material, and the volume change of both cathode and anode materials during cycling.

1.4.1 Cracking during heat-treatment

In order to optimize the power of the microbattery positive electrode, heat-treatment is required to provide transition energy for the crystallization of the as-deposited amorphous material. This post-annealing usually leads to the detachment of the films from the substrate and cracks on the surface of the film because of a difference in the thermal expansion coefficients.

1.4.2 Low conductivity of cathode materials

Cathode materials like $LiFePO_4$, have radically changed the focus of the lithium-ion battery community since its discovery in 1997.[15] This was the first positive electrode material that was environmentally friendly and made from plentiful elements, so as to reduce the potential cost of production of this compound, which has a theoretical capacity of 170 mAh/g. However, $LiFePO_4$ suffers from its limited high rate capability because of its intrinsically low electrical conductivity (10^{-9} S/cm).[15] In order to keep high energy density per footprint, a thicker film is needed for traditional 2D thin film microbattery electrodes, which will lead to a longer lithium ion diffusion distance and worsen the kinetics of the electrode.

1.4.3 Volume change of cathode and anode materials

Although the volume change of most cathode material is relatively small (~10%), due to the dense structure of deposited thin film microbattery electrodes, peel-off of the active material layer and film surface cracks still result in severe capacity fading during prolonged cycling. On the anode side, in order to pursue a higher specific

capacity and energy density, several single-phase and composite films based on reversible reactions of lithium have been proposed.

Tin possesses a high theoretical specific lithium capacity (994 mAh/g) and sodium capacity (847 mAh/g), and has been the focus of many investigations for both lithium-ion and sodium-ion batteries. Similar to silicon, to accommodate up to 4.25 lithium atoms and 3.75 sodium atom per tin atom, the tin structure undergoes a tremendous lattice expansion upon lithiation and sodiation: more than 360% and 520% volume expansion respectively.[16] This results in cracking and disintegration of the electrode, which lead to active material loss via reduced electronic contacted with the electrode and severe capacity loss. Moreover, tin particles tend to agglomerate once contact with each other, which leads to poor electrochemical performance of the anode.

1.5 Current techniques to enhance the microbattery electrodes

1.5.1 Annealing strategies and substrate modification

To reduce the cracking and film detachment during the heat-treatment process, different annealing strategies and modifications of substrate are applied. Dudney et al. suggested a lower annealing temperature and a longer annealing time,[9] Chiu's group applied heat-treatment in the deposition process.[17,18] Ti , Ag, Au and Pt layers were also deposited on the stainless steel as a buffer layer between the active material film and the substrate, which can improve the conductivity of electrodes.[19-21]

1.5.2 Co-deposition with conductive material

In order to achieve higher power, the conductivity of the positive electrode must be improved. Several conductive materials have been co-deposited with cathode materials. Eftekhari developed $LiFePO_4$- and $LiMn_2O_4$-Au film electrode by radio-frquency sputtering deposition.[22,23] Chung et al. synthesized $LiFePO_4$-Ag and $LiFePO_4$-C composite thin films by plasma laser co-deposition; the conductivity of the electrode at room temperature was estimated to be 10^{-7} and 10^{-3} S/cm respectively.[24,25] The increased conductivity implies that significant improvements to the electrode kinetics can only be made by the co-deposition method with the participation of expensive metals with high conductivities.

1.5.3 Nanoarchitectured 3D microbattery electrodes

The nanoarchitectured 3D technique can be considered as the most promising innovation of the microbattery electrode in recent decades. The 3D structure not only provides large surface area for a higher loading mass, but also creates intermediate space to accommodate the structural strains attributed to the electrode reactions during lithiation and de-lithiation. More importantly, it allows electrodes to lessen the diffusion length, thus providing greater power compared to 2D thin film electrodes.

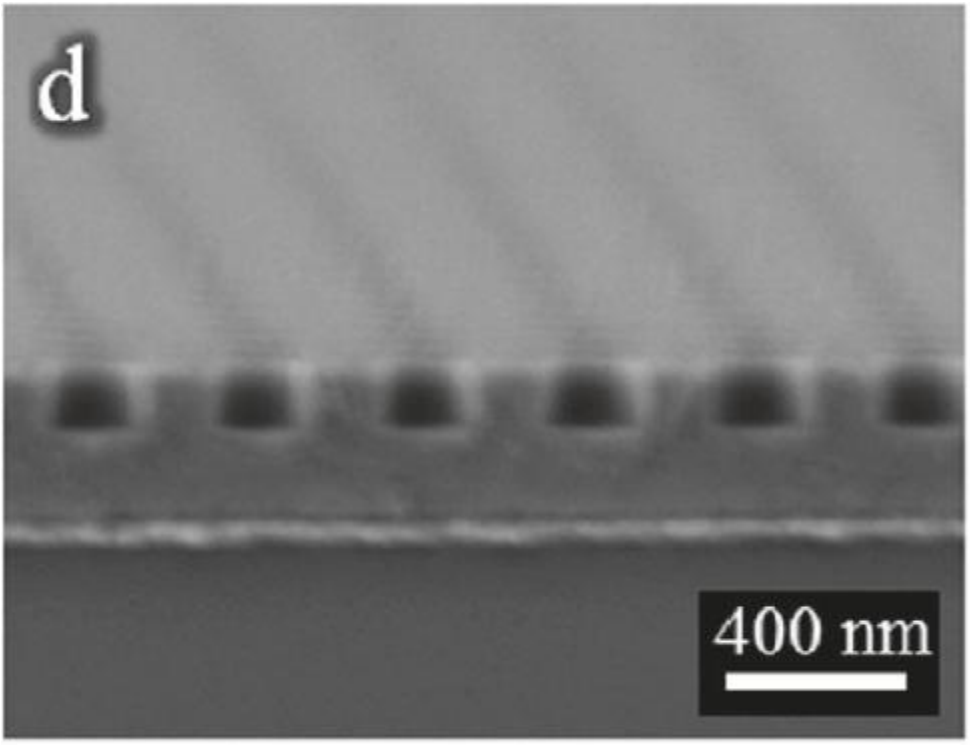

Figure 1.3 The cross-section SEM image of silicon electrode prepared by "Down Down" photolithography method.[26] Copyright 2011 American Chemical Society.

The fabrication method of 3D microbattery electrodes can be classified into "Bottom Up" and "Top Down". The "Top Down" method is derived from nanopatterning techniques including photolithography, nanoimprinting, electron beam lithography, and dip-pen writing. The process starts with the design of a nanopattern in the form of a mask, which is subsequently used for template etching or deposition to create 2D nanopatterns on a substrate. This has also been accomplished using laser interference lithography, which is a powerful method for fabricating periodic structures over large areas at the nanoscale level. Kim et al. produced carved silicon electrodes using the lithography technique under controlled exposure conditions, in combination with a dry etching process. (Figure

1.3) 2000 mAh/g specific capacity over 30 charge/discharge cycles was reported.[26]

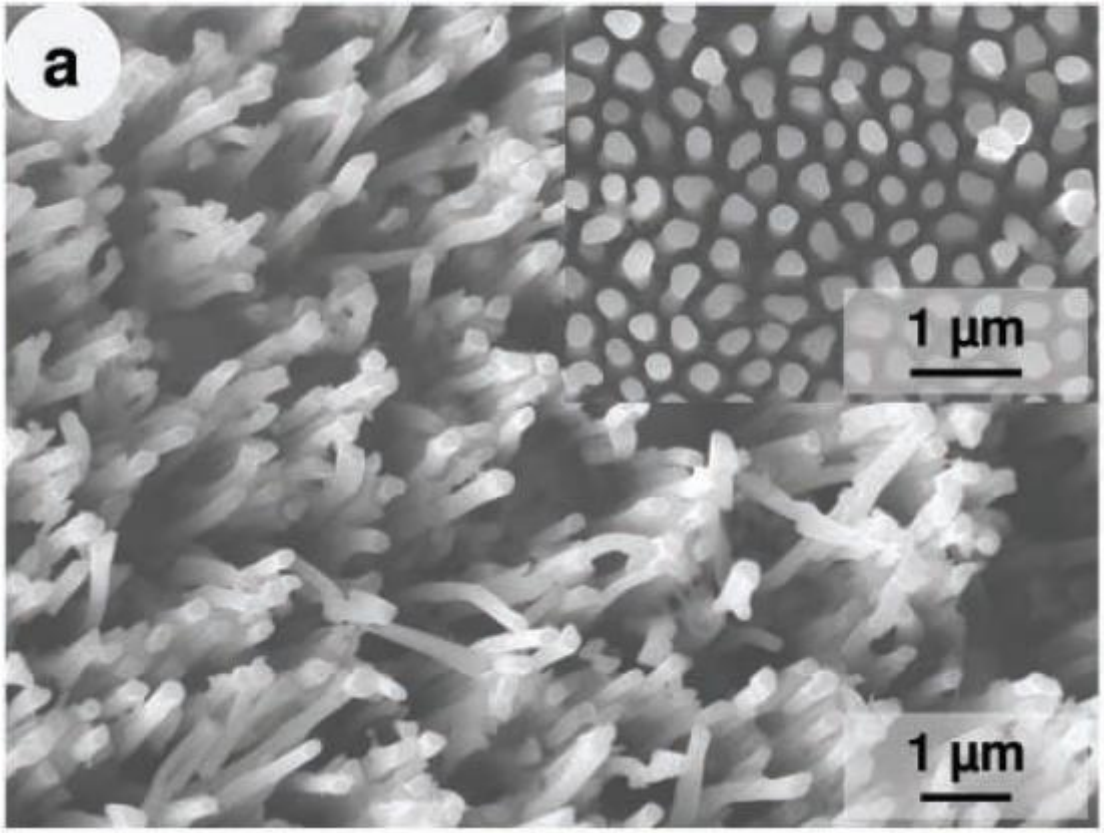

Figure 1.4 The SEM image of $LiCoO_2$ nanorods prepared by "Bottom Up" template method.[29] Copyright 2010 John Wiley & Sons, Inc

The fabrication of "Bottom Up" devices can be realized by template synthesis and standard depositions of electrodes onto nanostructured current collectors. The template synthesis is considered to be an effective approach for fabricating nanowires of a variety of materials. In particular, porous anodic alumina template has been widely used for fabricating nanowire arrays of metals, metal alloys, oxides, and semiconductors. Compared to conventional 2D thin film microbatteries, superior battery performance with improved areal capacity and rate capability has been demonstrated in straight nanowire arrays of Fe_3O_4/Cu, Ni-Sn/Cu, TiO_2/Al and

$LiCoO_2$/Al fabricated using templates.[27-30] However, the high cost of the template and the low loading mass limit the applications of this synthesis method: the price of one piece of alumina template with an 8 inche diameter exceeds 200 dollars, and the loading mass of the active material is on the scale of $\mu g/cm^2$. What's more, the high aspect ratio of the nanowire is not suitable for materials with low conductivity, because of the enlarged lithium ion transport distance by the 3D structure in the vertical direction.

Our group has successfully developed a 3D nanostructured current collector with more than tenfold surface area increase compared to 2D foil current collector. The vertical alignment of the nickel-coated virus rod on stainless steel discs is based on the genetically modified Tobacco mosaic virus and chemical deposition of nickel. Silicon has been deposited on the 3D current collector by chemical vapor deposition and aqueous electrodeposition. Core-shell nanowire structures have been established with enhanced kinetics of electrochemical reactions as well as higher reversible capacity.[31] This research, combined with the simplicity of the virus self-assembly and patterning process, represents a new strategy for the development of inexpensive and versatile synthesis techniques for energy-storage applications.

1.6 Objective of this research

The objective of the current research is to make a significant contribution to the advancement of both lithium-ion and sodium-ion microbattery technology. As alternative to lithium-ion chemistry, sodium-ion batteries have attracted increasing

attention, both because of the low cost associated with its high natural occurrences in both earth and ocean, and decent energy densities blessed by its similar chemical natures to lithium. Given this similarity, many mature electrode materials for lithium-ion chemistry have been investigated as drop-in replacement for sodium-ion; however, most of the efforts were rendered ineffective, as evidenced by the low capacities utilization, inferior rate capability, poor cycling stability or even complete electrochemical inactivity, for which the larger size of sodium-ion relative to lithium-ion is generally believed to be responsible. We believe the virus enabled 3D current collector can also play an important role in the improvement of sodium-ion chemistry

Specifically, the two main goals of the study are: (1) Apply TMV1cys structured 3D current collectors for radio-frequency deposited $LiFePO_4$ to fabricate a core-shell structure nanoforest cathode; characterizing and studying the effect of the 3D current collector on the rate capability, stability and impedance of the nanoforest cathode. (2) Employing physical vapor deposition and radio-frequency sputtering techniques to fabricate C/Sn/Ni/TMV1cys nanoforest anode for sodium-ion batteries; characterizing the anode and discussing how the virus enabled 3D structure and carbon coating improved the stability of the anode.

The subsequent four chapters discuss the efforts to achieve the stated goals. Chapter 2 describes the experimental procedure for fabricating the TMV1cys structured 3D current collector. Chapter 3 focuses on the fabrication of a virus enabled $LiFePO_4$ 3D electrode and its characterization as well as the analysis of the electrochemical performance. Chapter 4 investigates the morphology and performance of physical vapor deposited tin on the viral 3D template as negative

electrode for sodium-ion batteries. Chapter 5 includes the conclusion of this thesis paper and the discussion of future work.

Chapter 2. Virus Enabled 3D Current Collector

2.1 Introduction

The cross-section between biology and nanotechnology creates a growing interest in developing the self-assembly and inorganic binding capabilities derived from biological materials for use in device and energy storage development. Specifically, the genetic tractability of Tobacco mosaic viruses (TMV) has been utilized to create novel bio-inorganic interfaces.[32] Cylindrical viruses rods have been structured into conductive nano-wires, sensors, memory devices and battery electrode materials by taking the advantages of thess novel interfaces[33]. Our group has developed TMV as a promising bio-inorganic template which can be easily patterned on the surface of metal substrates to form nano-scaled 3D structures. [31]

TMV is a cylindrical high aspect ratio particle, composed of ~2100 identical coat protein subunits assembled onto a positive strand of genomic RNA to produce a nanorod with 300 nm in length, 18 nm in diameter and containing a 4 nm inner channel. Our previous studies have shown that the genetic addition of a cysteine (cys) residue at N-terminus of each coat protein subunit allows for the self-assembly of this engineered virus, TMV1cys, onto metal surfaces through the near covalent-like interaction between the thiol group of the introduced cysteine and the metal atoms. Since this interaction is only possible with the cysteine residues exposed at the end of the cylindrical rod, a nearly vertical assembly of these virus particles ensues,

producing a nanoforest of assembled virus templates.[31] Virus assembled nano-features produced a 13 to 80 fold increase in reactive surface area depending upon virus concentration. Incorporation of these surfaces into simple nickel-zinc micro-batteries also improved performance compared to planar electrode geometries.[31, 33]

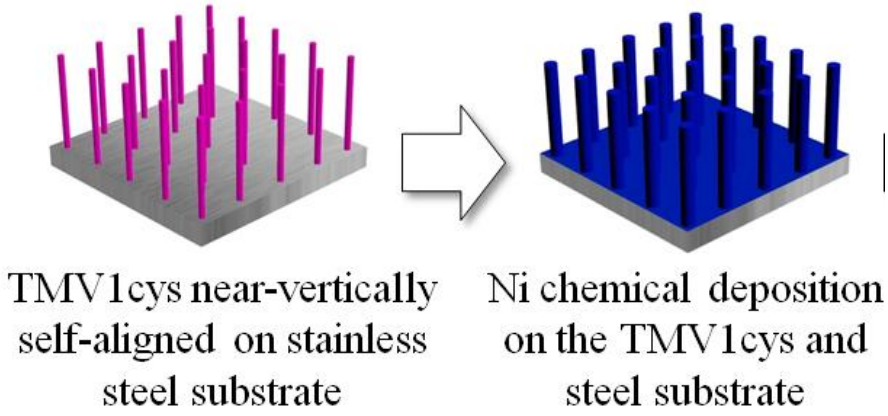

Figure 2.1 The two main steps in the preparation of the virus enabled 3D current collector: TMV1cys self-assembling and nickel chemical deposition.

2.2 Experimental

The synthesis process of 3D TMV1cys templates includes the TMV1cys self-assembly and chemical nickel coating.(Figure 2.1) Beginning with the TMV1cys self-assembly, the polished stainless steel discs were immersed into 0.1g/L TMV1cys solution with 0.1M sodium phosphate buffer with a 7 pH value for at least 48 hours, the virus will attach on the entire stainless steel surface near vertically. The positioning of the 1cys thiol group contributes to the attachment and vertical positioning of the viral rods onto metal surfaces. Although surface exposed, the 1cys residue is recessed within a groove and partially covered by the C-terminal arm of the coat protein. This position likely inhibits direct contact between the cysteine derived

thiol and a surface except at the 3' end of the virus rod where the thiol group is sufficiently exposed to make direct surface contact, which leads to 3D electrode arrays in nearly vertical manner. Then the discs were moved to palladium catalytic solution (Na_2PdCl_4). In this step, the surface-assembled TMV1cys were activated with palladium catalytic clusters via the reduction of Pd^{2+} to Pd^{0} on the exposed cysteine residues using a hypophosphite reducing agent.[32] Following this process, nickel is deposited on the Pd^{0} activated virus surface in an electroless plating solution. Activated TMV1cys templates are put into a 0.1M $NiCl_2$ plating solution for 5 minutes with the addition of 0.5M $(CH_3)_2NHBH_3$ (Dimethylamine borane, DMAB) as a reducing agent. After nickel deposition, the samples were dried overnight in a vacuum oven at $120^{o}C$ to evaporate any water left on the surface and avoid oxidation. Most TMV1cys attach on the stainless steel surface vertically or near-vertically due to the surface roughness. Few TMV1cys lay down on stainless steel because there is clearly some flexibility in this attachment and in the virus rods themselves when the virus rods are attached to the rough surface from one end. Due to the self-alignment of two or three TMV1cys particles in the assembly process, the length of surface attached TMV1cys rods vary from 300 nm for a single TMV1cys to 900 nm for three aligned TMV1cys. Based on the metal coating thickness from previous work (20-40 nm), the average length of nickel coated TMV1cys rod is ~600±300 nm.[33] Coated surfaces remained stable even after vigorous rinsing to remove excess plating solution.

Chapter 3: Architecturing Hierarchical Function Layers on Self-Assembled Viral Templates as 3D Nano-Array Electrodes for Integrated Li-ion Microbatteries

3.1 Introduction

Since the birth of Li-ion battery two decades ago, its energy/power density and cycling stability have been significantly advanced, thanks to both innovations in materials and optimization of cell engineering. This young battery chemistry in either prismatic or cylindrical configurations --- both of 2D character --- has dominated the multi-billion dollar market of portable electronics as the rechargeable power source of choice, and is posing to prevail in more lucrative and strategically significant markets of automotive and stationary grid-storage applications. However, to a much lesser degree have these advances benefitted the on-board power needs of micro-electronics, another fast-growing market of billion dollar scale, where amount of energy stored on given footprint (J/mm^2) precedes that in either unit weight (Wh/Kg) or volume (Wh/L), and, more importantly, where the capability of battery active components being integrated as part of the integrated circuit (IC) during micro-fabrication process would prove a more superior advantage in manufacturability. Hence, in those micro-/nano-electromechanical systems (MEMS/NEMS) or bio-medical devices, the desired on-board power delivery in exceptionally small geometric scales often meets the distinct challenge of accommodating the clumsy battery configurations of 2D nature that were originally designed for devices thousand or even million times larger in

dimension. Furthermore, most conventional Li-ion battery key components (electrolytes, separators) cannot survive the integration process during the micro-fabrication process, characterized by the solder-reflow operation (260 ^{o}C). Even the solid thin film Li-ion batteries, although more amenable toward micro-fabrication process than liquid electrolyte Li-ion technology, are constrained by the Li melting point (180.6 ^{o}C), not to mention that their typical low power densities, mainly imposed by LiPON electrolyte and its limited reaction interface with electrodes, often fall short of the pulse demands of MEMS/NEMS devices. To address this shortcoming of thin film battery technology, Si-Li alloys has been recently explored as an alternative anode for micro-batteries,[34] while various top-down processes familiar to IC industry have been employed to design, assemble and pack nano-structured electrode arrays.[35]

Approaching the challenge from a new avenue, the present work attempts to leverage a cathode technology, $LiFePO_4$, which has been matured by Li-ion industry as safe, low cost and high power density chemistry in conventional battery designs, as a potential active cathode for 3D nanoelectrode arrays. Bottom-up instead of top-down approaches was adopted, so that not only on-site manufacturability complying to IC micro-fabrication is allowed, but also the usual challenge of high ionic/electronic resistance in nanometric scales could be readily resolved by precisely arranging multilayer of active and auxiliary materials over vertically-assembled bio-templates, i.e., genetically-modified clones of tobacco mosaic virus (TMV). The sophisticated micro-mechanism architectured in such manner stores and delivers

energy at excellent rate and efficiency as result of the synergistic collaboration of these various layers of materials.

Previously we have successfully used a similar but much simpler approach to fabricate a self-aligned 3D Si nano-anode arrays.[31] The coupling of these anode and cathode chemistries enabled by the current bottom-up nano-hierarchical technique would eventually pave the way to fabricate an all-solid-state 3D $LiFePO_4$/LiPON/Si nanoforests micro-battery.

The primary challenge encountered by a 2D-nature electrode in MEMS configuration is the limited footprint (usually in m^2). To maximize the active sites for energy storage per geometric area, one will be forced to seek space in the third dimension, leading to investigations of 3D design for microelectrode arrays.[35] A logic development of this approach leads to the architecture of rod-like structures that would stand vertically on the substrates while loading active components with its much heightened surface area. Recent advances in nanomaterial engineering have enabled diversified routes to such nanorod preparations, and an increasingly number of mature cathode chemistries from conventional Li ion industry has been applied. However, an intrinsic challenge stemming from the high aspect ratio of rod-like structures would be the new kinetic control for the intrinsically poor electronic conductor $LiFePO_4$, which affects the rate of power delivery. Although the increased electrolyte/electrode contacts in these 3D electrode designs significantly facilitates "ionic transfer" by reducing tortuosity in migration pathway, the electron transfer between the current collector and $LiFePO_4$ active species, on the other hand, has to occur through a longer pathway along the elongated shape of the $LiFePO_4$ rods,

which is hampered by the usually very high aspect ratio of these rods, and further slowed down by the phase transformation between $FePO_4$ and $LiFePO_4$ along the rods during the reversible lithiation and de-lithiation. A recent work, where 3D $LiFePO_4$ nanorods are directly self-aligned on current collectors by using a template, typically exemplified this new challenge.[36] The elongated electronic migration distance and the small contact area between the active species and the main current collector significantly reduce the reaction kinetics of the cell chemistry, which was worsened by the low intrinsic electronic conductivity of $LiFePO_4$. In addition, mechanical stresses induced by lithiation at the interfaces between the nanorods and the current collector could also lead to fracturing upon long term cycling, adding further barrier to reaction kinetics in these electrodes.

An effective solution to the above issues, which is intrinsic to all rod-like architectures, would be the insertion of an electronically conductive metal-core within the rods, which serves as an intimate electronic pathway between the active species on the stem of the nanorods and the main current collector at the terminal. Such a metal-core would function as a built-in "nano-current collector" that effectively facilitates "electronic transfer", thus accelerating the electrochemistry reaction rate. Since the metal-core is directly rooted onto the main current collector, it can also effectively relieve the stresses of lithiation/de-lithiation and maintain the integrity of the nanorod, both mechanically and electronically, at high reaction rates and over extend use. Previously, such a metal-core has been fabricated using sacrificed nano-structured templates through a wet impregnation process, followed by etching or template decomposition.[37,38] However, the complexity of that practice and the

associated high processing cost would limit its scalability, especially if it is considered as part of the fabrication as MEMS/NEMS power. Hereby we propose a "bottom-up" approach using biological templates to achieve the $LiFePO_4$-nanorods with central metal cores. The genetically-modified tobacco mosaic virus (TMV) proves to be a convenient and reliable template that is not only stable but also amenable toward magnetron deposition processes, hence allowing architecturing of sophisticated multilayer energy storage mechanisms.

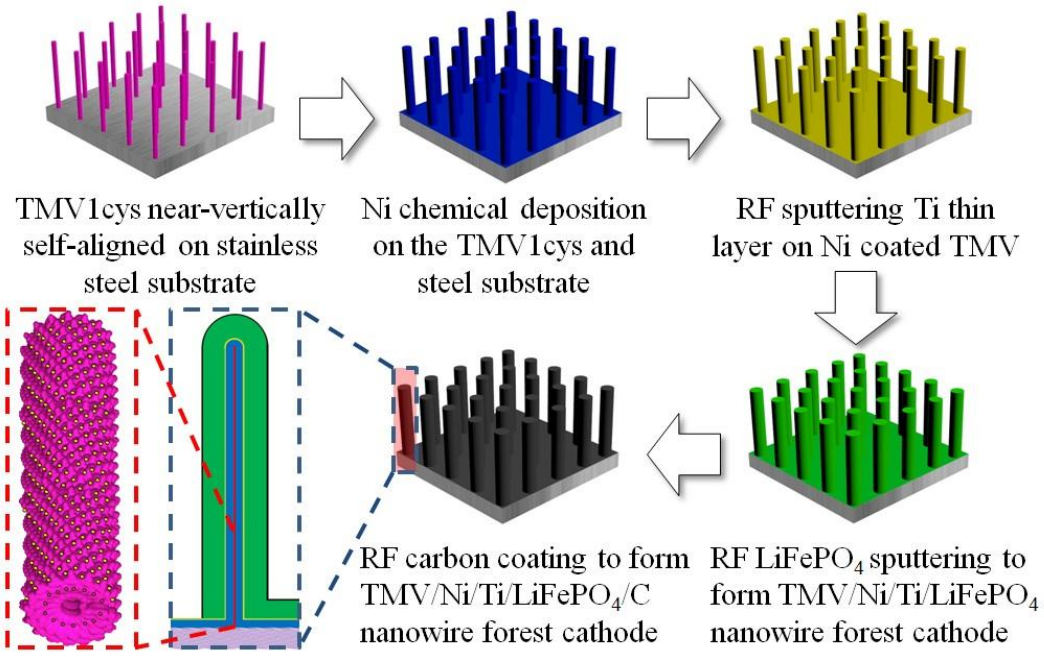

Figure 3.1 Schematic description of TMV-templated near-vertical assembly of $LiFePO_4$ nanoforest on current collector with multi-layered nano-hierarchical arrangement of active materials and electron conducting pathway.

TMV is a cylindrical high aspect ratio particle, composed of ~2100 identical coat protein subunits assembled onto a positive strand of genomic RNA to produce a nanorod with 300 nm in length, 18 nm in diameter and containing a 4 nm inner

channel. Our previous studies have shown that the genetic addition of a cysteine (cys) residue at N-terminus of each coat protein subunit allows for the self-assembly of this engineered virus, TMV1cys, onto metal surfaces through the near covalent-like interaction between the thiol group of the introduced cysteine and the metal atoms. Since this interaction is only possible with the cysteine residues exposed at the end of the cylindrical rod, a nearly vertical assembly of these virus particles ensues, producing a nanoforest of assembled virus templates,[32,33] as shown schematically in Figure 3.1. More importantly, the presence of cysteine residues enables metal coatings at the virus surface via electroless plating, producing a conductive metal nanoshell around the TMV1cys core. It is important to emphasize that, differing from the pioneering bio-template techniques employing engineered M13 bacteriophage templates to bio-mineralize amorphous a-$FePO_4$ nanowire powders, while the a-$FePO_4$ nanowire cathodes still have to be fabricated through ink-casting of mixture of binder, carbon black and a-$FePO_4$ nanowires,[39,40] the present approach results in a direct assembly and fabrication of 3D nanoforest electrode arrays, which already possess the necessary composite ingredients including a built-in 3D nano-current collectors and carbon conductive sub-layer but in absence of polymer binder. This unique "bottom-up" can be easily scaled up at low cost or integrated with IC processes.

3.2 3D C/$LiFePO_4$/Ti/Ni/TMV1cys nanoforest cathode preparation

As the templates of microelectrode arrays, TMV1cys clones were self-assembled onto a stainless steel (SS) current collector in aqueous solutions (Figure

3.1a) as described previously, which is sequentially followed by chemical deposition of nickel (Ni) in an electroless plating bath to form a 3D current collector (Figure 3.1b), radio-frequency (RF) magnetron sputtering depositions[17,41] of Titanium (Ti) (Figure 3.1c) and $LiFePO_4$ sub-layers, respectively, to form the multi-layered $LiFePO_4$/Ti/Ni/TMV1cys nanoforest (Figure 3.1d). Eventually, a ~1.65 mg loading mass (1.06 mg/cm^2) of $LiFePO_4$ is obtained, and then the annealing at 500^{o}C for 1 or 2 hours to crystallize the active species. The Ti sub-layer between Ni and $LiFePO_4$ is designed for the following purposes: (1) to prevent the electrochemical oxidation of Ni during charging, because the anodic oxidation of Ni occurs near the operating voltage of $LiFePO_4$ (3.5 V vs. Li); (2) to alleviate Ni diffusion into $LiFePO_4$ during the high temperature annealing process;[41] and (3) to enhance adhesion between $LiFePO_4$ and the "nano-current collectors" as a means to minimize potential capacity loss induced by the mechanical stresses that occurs during electrochemical lithiation/de-lithiation.

The $LiFePO_4$ and Ti layers were deposited sequentially on stainless steel (SS) discs (15.5 mm in diameter) containing preassembled Ni coated TMV1cys templates by ultrahigh vacuum magnetron sputtering under continuous vacuum. The SS discs were polished carefully and cleaned by sonication in alcohol and acetone before loading into the vacuum chamber. The patterned 3D TMV1cys templates and Ni coating were done as previously described. The synthesis process of 3D TMV1cys templates was described in Chapter 2. A $LiFePO_4$ (99.95%, purity) and Ti (99.995%, purity) were used as targets (76.2mm in diameter). The target area was pre-sputtered to remove impurities by applying 100W RF power under Ar (purity of 99.99%) for 20

min prior to film deposition. Briefly, the sputtering was conducted in an Ar atmosphere (0.3 Pa for Ti and 1 Pa for $LiFePO_4$) using a power density of 6.0 W/cm^2 for the Ti layer (direct current power) and 1.5 W/cm^2 for $LiFePO_4$ (RF). The target-to-substrate separation was 8 cm. The substrate temperature during film growth was ~250 ℃ (due to plasma heating). In comparison, $LiFePO_4$/Ti/SS film stacks were also prepared under the same conditions and the multilayer thickness confirmed by TEM. After deposition, the samples were annealed in a vacuum furnace at 500^{o}C for 1 and 2 hours. In order to improve the sample performance carbon sputtering was applied to the 2 hour annealed $LiFePO_4$/Ti/Ni/TMV1cys sample with a 4.5W/cm^2 power density at a 1 Pa Ar atmosphere for 20 min.

3.3 Characterization of the 3D $LiFePO_4$ nanoforest cathode

The $LiFePO_4$ loading mass of each sample was measured by high-precision microbalance (Mettler Toledo, XS105 dualRange) within an accuracy of 1 μg. X-ray diffraction (XRD) measurements were performed to ascertain the crystallographic structure of the film stacks using a BRUKER AXS diffractometer with Cu-Kα radiation source operated at 40 kV and 50 mA. Raman scattering spectrum were collected by Horiba JobinYvonLabRAM Raman microscopes (models ARAMIS) with 633nm excitation line. The surface morphology of the samples was characterized by scanning electron microscopy (HITACHI SU-70 and S-4800). A high-resolutiontransmission electron microscopy (HRTEM, JOEL JEM 2100F) with an energy-dispersive spectrometer (EDS) was employed to analyze the microstructures and interface characteristics of the film stacks.

3.3.1 SEM

This multi-layered composite nanoforest assembly is subsequently coated with an additional sub-layer of carbon (C) ~8 nm in thickness (Figure 3.1e). To electronically wire the outside C coating layer with inner Ni current collector, three small masks in the area of 0.04 cm^2 was placed on 3D Ti/Ni/TMV1cys template before the $LiFePO_4$ deposition. These masks were then removed during the carbon deposition, creating direct pathways between the potential electrochemical reaction fronts and the main current collector.

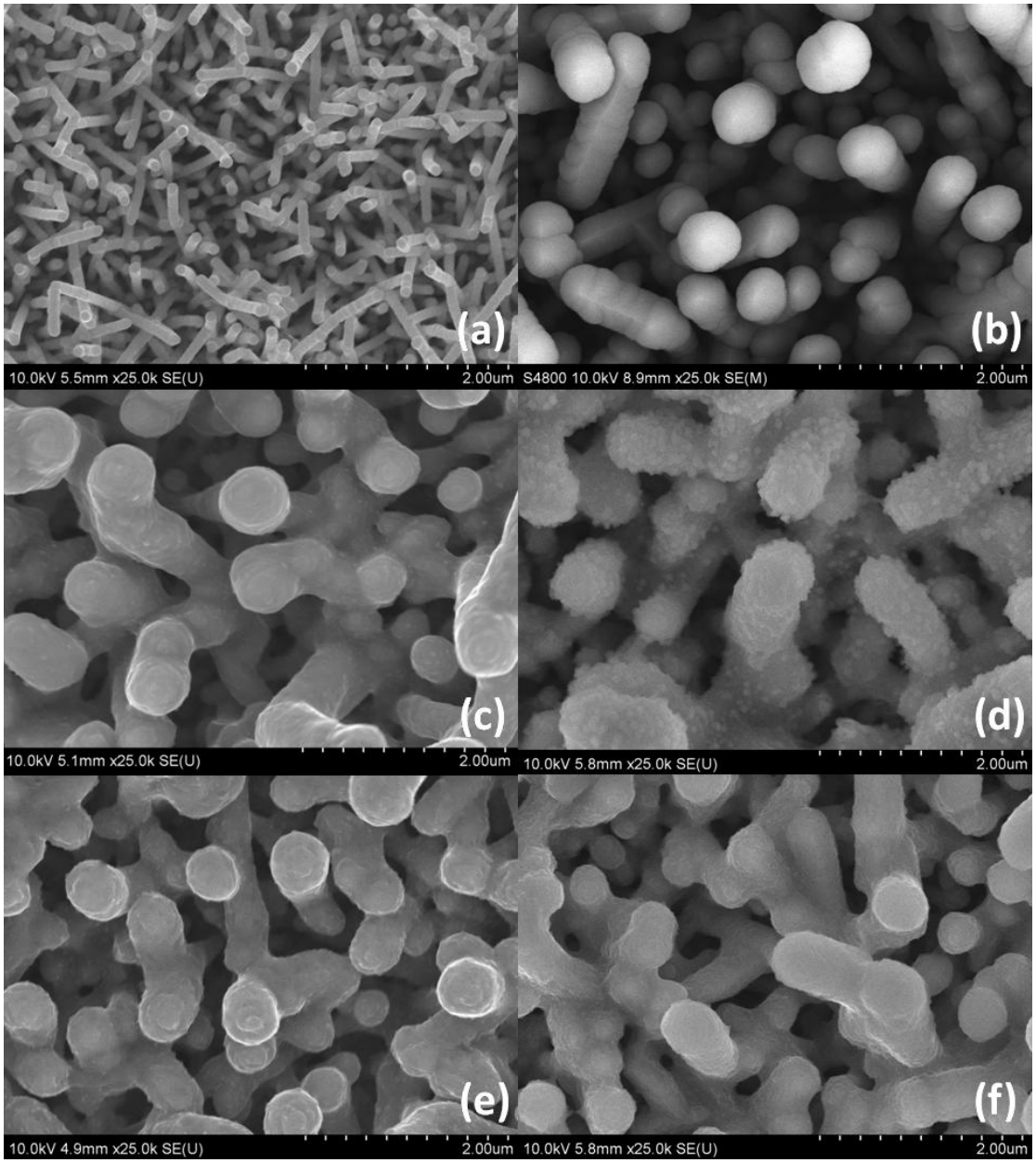

Figure 3.2 The SEM images of the (a) Ti/Ni/TMV1cys on stainless steel, (b) as-deposited $LiFePO_4$/Ti/Ni/TMV1cys, (c) annealed $LiFePO_4$/Ti/Ni nanowire at 500^oC for 2 hours, (d) annealed $LiFePO_4$/Ti/Ni nanowire after 450 charge/discharge cycles at 1C rate, (e) carbon coated annealed $LiFePO_4$/Ti/Ni nanowire, (f) carbon coated annealed $LiFePO_4$/Ti/Ni nanowire after 450 charge/discharge cycles at 1C rate.

The above fabrication sequences are individually monitored with scanning electron microscopy (SEM) images. As shown in Figure 3.2a for the Ni coated TMV templates, the highly dense forest of Ni/TMV1cys nanorods are arranged on the SS surface in nearly-vertical manner, while some TMV1cys self-guide themselves into making longer nanocolumns. The subsequent depositions of Ti and $LiFePO_4$ on these templates forms uniform layers around the rod shaped particles. The final $LiFePO_4$/Ti/Ni/TMV1cys multilayer nanorods have an average of ~500 nm in diameter and >2.5μm in length (Figure 3.2b). The thickness of $LiFePO_4$ coating (~200 nm) is 7 times thicker than $LiCoO_2$ layer on Al nanorodes,[29] 12 times of ALD TiO_2 coating on Ni nanorods,[42] and 10 times of $LiFePO_4$ nanorods on Pt.[17]

3.3.2 XRD

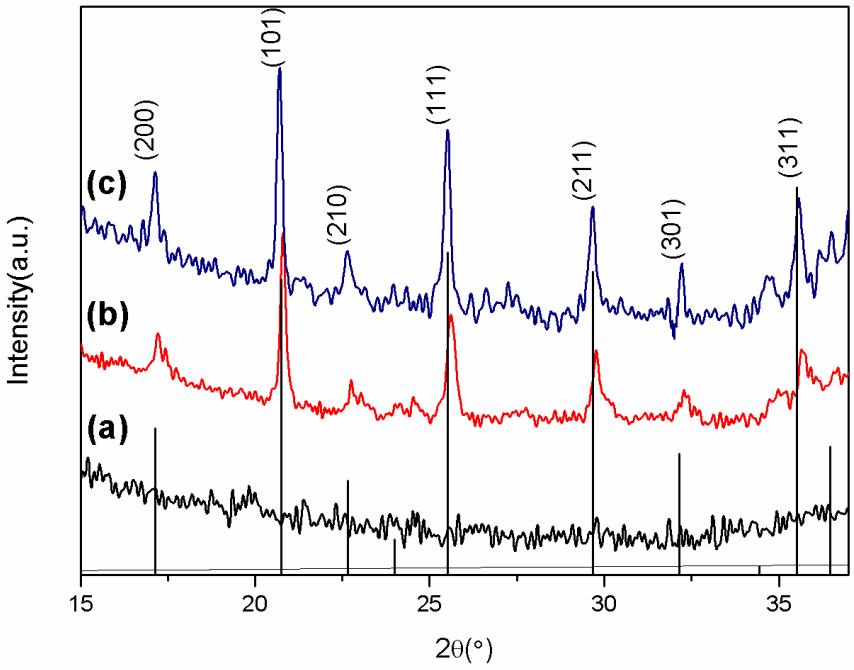

Figure 3.3 The XRD patterns of (a) as-deposited $LiFePO_4$nanwire forest, (b) annealed at 500°C for 1 hour in vacuum, (c) annealed at 500°C for 2 hours in vacuum. All the peaks in Figure 3.3 are indexed based on the XRD data base file (JCPDS-832092).

The as-deposited $LiFePO_4$ nanorods give no apparent diffraction peaks in its X-ray diffraction (XRD) pattern (Figure 3.3) indicating its amorphous nature. After heat-treatment at 500°C for 2 h under vacuum, the smooth surface of the nanorods (Figure 3.2b) becomes visibly rougher, induced by the phase changes from amorphous to crystalline olivine structure (space group pnma) that occurs during the annealing treatment (Figure 3.2c), as evidenced by the XRD patterns in Figure 3.3. Although the protein-based core of TMV1cys might have been decomposed into inorganic species during this high temperature process, the robust $LiFePO_4$/Ti/Ni

shell maintains structural integrity. The virus functions only as a scaffold for the electroless deposition of nickel. Under the conditions used we reported the deposition of ~ 10^{-4} g/cm^2 of nickel on the surface of similar virus-assembled electrodes. Weight contributions from the virus were found to be negligible. In addition the thickness of the nickel coatings are nearly twice as that of the virus core. Thus, the virus makes up only a small fraction of the assembled nickel surface. Based on this, we anticipate that carbonization of the virus within the nickel shell would have little if any impact on the nickel structure or its overall make up. In Figure 3.2e, the carbon coated $LiFePO_4$ nanorods are shown to have morphology similar to that of the carbon-free $LiFePO_4$ nanorods, with a rather uniform carbon film.

3.3.3 TEM and EDS mapping profile

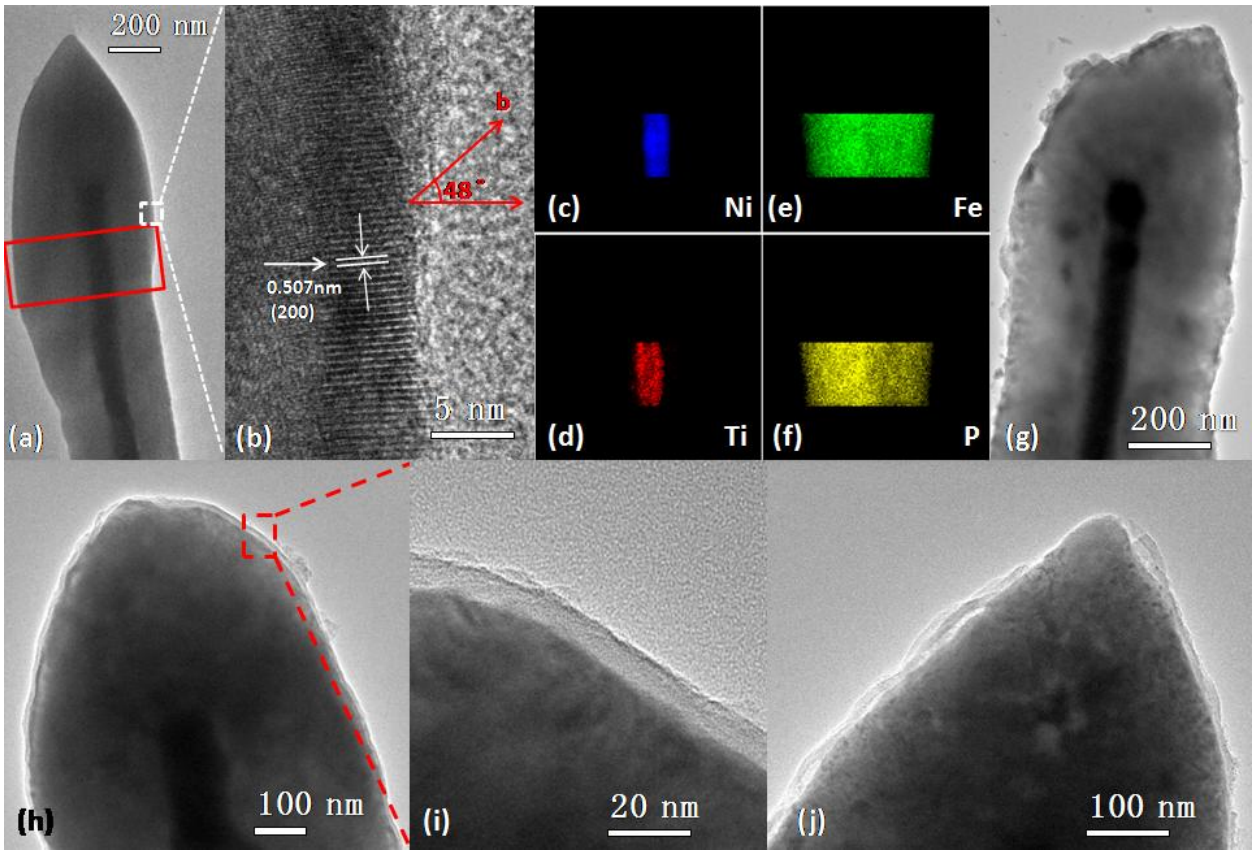

Figure 3.4 (a) TEM image of $LiFePO_4$/Ti/Ni nanowireafter annealing at 500^oC for 2 hours, (b) the high-resolution TEM image of the $LiFePO_4$ crystal. The EDS mapping profiles in the red mapping rectangle marked in (a) for Ni (c), Ti (d), P (e), and Fe (f). Li-ion diffusion channel (b axis direction) is marked in (b). (g) TEM image of $LiFePO_4$/Ti/Ni nanowire after 450 cycles at 1C rate. TEM image of C/$LiFePO_4$/Ti/Ni nanowire (h) before charge/discharge cycle, (i) enlarge figure of (h), (j) after 450 charge/discharge cycles at 1C rate.

The structure and thickness of each layer in a single $LiFePO_4$/Ti/Ni nanorod after annealing are demonstrated in the transmission electron microscopy (TEM) images and energy dispersive spectroscopy (EDS) element mapping in Figure 3.4, in

which the hierarchy of Ti/Ni metal nanorods of ~80 nm in diameter and the $LiFePO_4$ shell of ~200 nm in thickness are clearly visible (Figure 3.4a).

Both SEM (Figure 3.2) and TEM (Figure 3.4) images cooperatively indicate that within each $LiFePO_4$ nanorod there is a Ti/Ni core that directly connects to the SS main current collector. Thus, the virus-assembled nanoforests carry nearly-uniform $LiFePO_4$ coatings (Figure 3.4a), whose novel multilayered architecture would allow the active shell $LiFePO_4$ to maintain an intimate electrical connection along the entire length of the nanorod during the electrochemical lithiation/de-lithiation. This intimacy on nanoscale is usually a challenge for such high aspect ratio configurations and has been the main reason for most degradation of electrochemical performances over long-term cyclings. The lattice spacing of the $LiFePO_4$ nanocrystalis marked in Figure 3.3b, which is in accordance with the (200) plane.

A layer-by-layer structural analysis of the annealed $LiFePO_4$ nanowire was further performed by EDS element mapping as shown in Figure 3.4c-f, which demonstrated that the 10 nm Ti sub-layer effectively suppressed the diffusion of the Ni (~50 nm thick) into the $LiFePO_4$ layer (~200 nm), and thus prevents the Ni sub-layer from oxidation during charging and minimizes its potential contribution to the irreversible capacity. On the other hand, similar to aluminum (Al), Ti qualifies as an excellent current collector for cathode due to its high stability against oxidation. Therefore the slight diffusion of Ti into both $LiFePO_4$ and Ni sub-layers, while enhancing the mechanical stability of the cathode nanorods, does not affect electrochemical stability. Again, consistent with SEM, the decomposition of the TMV1cys inner core during annealing at 500^oC does not lead to any discernible

structural disintegration of $LiFePO_4$/Ti/Ni nanorods (Figure 3.4a). As interior of the nanoforest electrode arrays, the possible remnants of TMV1cys might consist of largely carbonized amorphous mass doped with heteroatoms (O, N, S and P etc), which are expected to remain inert during electrochemical reactions. Overall the Ti/Ni nanoshell connected to the SS current collector provides a rather facile electronic transfer pathway across the entire $LiFePO_4$ nanorod; additionally it might also act as a robust backbone that strengthens the mechanical integrity of the electrode arrays upon repeated electrochemical cyclings.

3.3.4 Raman spectra

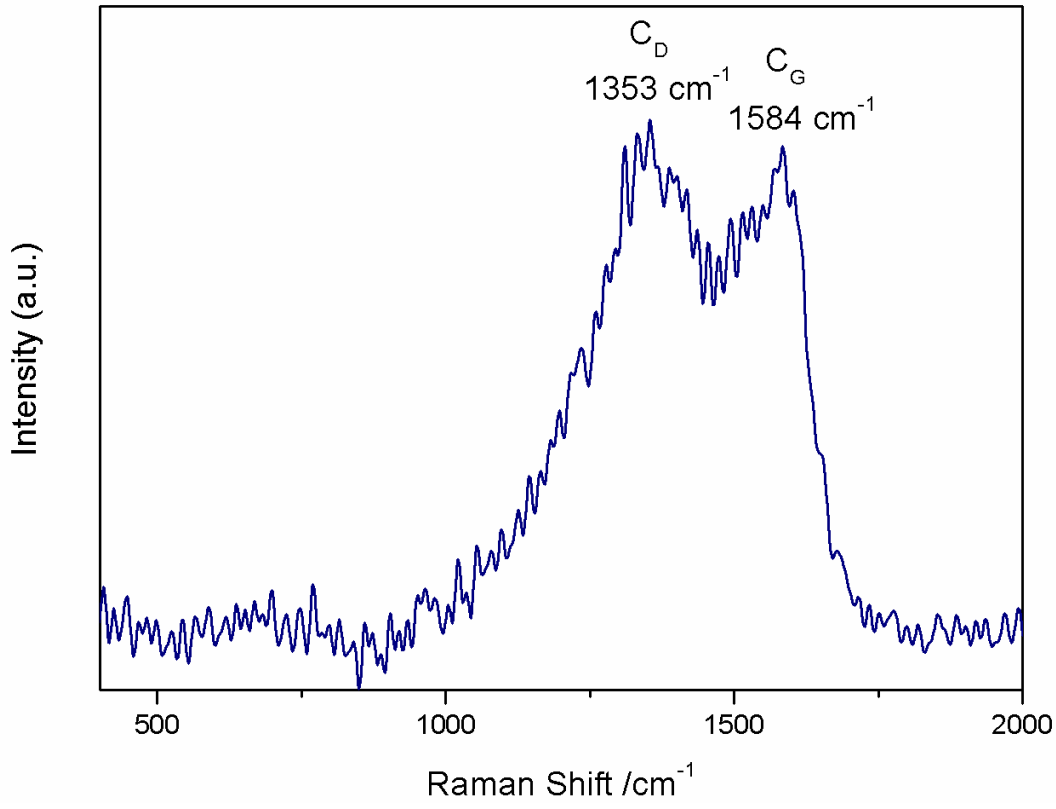

Figure 3.5 Raman spectrum of the carbon coated $LiFePO_4$/Ti/Ni nanowire forest cathodes.

After a single carbon coating, TEM images show that a C sub-layer of ~8 nm is uniformly deposited along the $LiFePO_4$/Ti/Ni composite nanorods. The graphitization degree of the carbon layer can be estimated from the characteristic wide D and G bands in the Raman spectrum at around 1350 and 1600 cm^{-1} (Figure 3.5), between which the former (D band) is correlated with structural defects- and disorder-induced features in the graphene layers of carbon materials, while the latter (G band) is indicative of the high-frequency E_2g first-order graphitic crystallites of carbon.[43-45] The presence of the strong D band suggests that the carbon component on the C/$LiFePO_4$/Ti/Ni nanorods have low crystallinity that is typical of disordered graphitic material. No peaks of Fe-O and PO_4^{3-} are detected, confirming that the carbon sub-layer fully and uniformly covers the surface of the $LiFePO_4$/Ti/Ni nanoforest.

3.4 Electrochemical tests result and discussion

Electrochemical performance of the $LiFePO_4$ cathodes were tested in coin cells (R2032) using Li foil as a counter electrode and a 1 M $LiPF_6$ solution in ethylene carbonate/diethyl carbonate (EC/DEC, 1:1 by vol. %) as electrolyte. The charge/discharge testing was carried using an Arbin BT-2000 battery test station over the voltage range of 2.7-3.6V versus Li/Li^+. All electrochemical experiments were conducted at room temperature and all capacity values were calculated based on the weight of the $LiFePO_4$. Electrochemical impedance spectra (EIS) were collected using a Solartron 1260/1287. Cells were tested at the 50^{th} and 450^{th} charge/discharge

cycle with charging set to 3.6V with a 2 hour rest and a scan range from 10^6 Hz to 0.01 Hz.

3.4.1 Rate capability

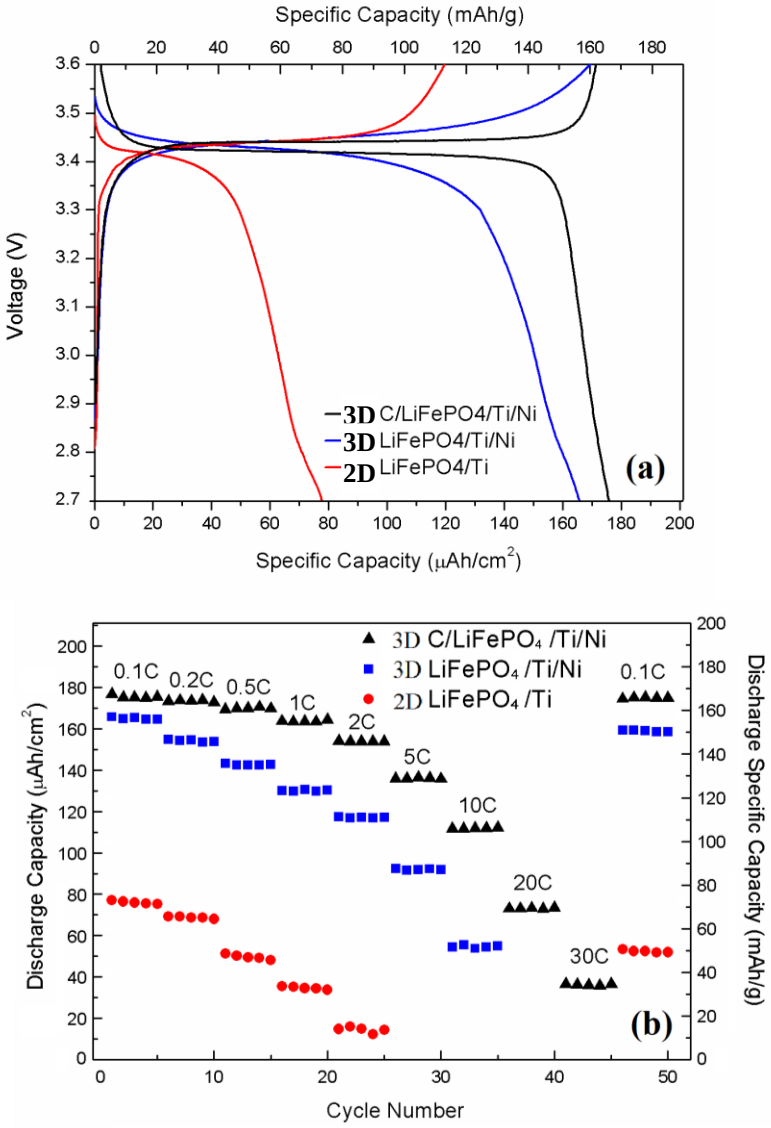

Figure 3.6 (a) The potential profiles of C/$LiFePO_4$/Ti/Ni, $LiFePO_4$/Ti/Ni nanowire forest cathodes, and $LiFePO_4$/Ti thin film cathode 0.1C charge/discharge current, and (b) rate performance of 3D C/$LiFePO_4$/Ti/Ni, 3D $LiFePO_4$/Ti/Ni nanowire forest cathodes, and 2D $LiFePO_4$/Ti thin film cathode at different charge/discharge currents.

The electrochemical performance of 3D $LiFePO_4$/Ti/Ni nanoforest cathodes with and without a carbon sub-layer were tested in coin cells with typical liquid electrolytes and compared to the performance of reference, a 2D $LiFePO_4$/Ti/SS multi-layer thin film cathode that was deposited under the same conditions but in the absence of the TMV1cys template. The $LiFePO_4$/Ti/Ni nanoforest cathodes have the same active loadings as the 2D $LiFePO_4$/Ti thin film cathodes, but the thickness (~600 nm) of $LiFePO_4$ sub-layer in the latter was three times larger than that (~200 nm) on its 3D counterpart due to inherent high surface area of the latter. Figure 3.6a shows the charge/discharge voltage profiles of two 3D $LiFePO_4$/Ti/Ni nanoforest cathodes, with and without a carbon coating, in comparison with the 2D $LiFePO_4$/Ti thin film cathode at 0.1C. Both charge and discharge profiles show reversible electrochemical reactions at voltage plateaus around 3.4 V, which is the characteristic phase transition between $FePO_4$ and $LiFePO_4$. The 2D $LiFePO_4$/Ti thin film cathode delivers 78 $\mu Ah/cm^2$, only 53% of its theoretical capacity; in contrast, the TMV-assembled $LiFePO_4$/Ti/Ni nanoforest composite cathodes, containing the same active loading but only 1/3 the thickness of the $LiFePO_4$ thin film cathodes, delivered a discharge capacity of 162 $\mu Ah/cm^2$ (158 mAh/g). Thus the nanoforest architecture produced up to 93% of the $LiFePO_4$ theoretical capacity, obviously benefiting from the shortened distances for both ionic and electronic migration present within the virus template nanorods. Carbon coating on $LiFePO_4$/Ti/Ni nanoforests further enhanced the capacity utilization of active species to 98% of the theoretical value.

Among the three cathodes studied, the 3D C/$LiFePO_4$/Ti/Ni nanoforest composite also presents the smallest potential hysteresis between the charge and discharge voltage plateaus, indicating a facile reaction kinetics within this cathode architecture.The flat potential plateau of the carbon coated $LiFePO_4$ nanoforest composite cathode is obviously due to strong Li-polaron coupling that causes Li-ions and electrons to migrate together in an olivine lattice,[46] thus the enhancement of the electronic conductivity by carbon coating also increases the Li-ion mobility while reducing diffusion overpotential during phase change.

TMV1cys enabled 3D $LiFePO_4$/Ti/Ni nanoforest arrays not only enhance the capacity utilization at a low charge/discharge current, but also significantly increase its overall rate performance at higher current densities, which is of particular importance to pulse performances often required in MEMS/NEMS applications, where the capability of electrodes to capture and release energy at fast rates determines efficiency and electrode life. To evaluate the effect of this nano-architecture on fast electrochemical reaction kinetics, the nanoforest cathodes under investigation were subjected to a rather abusive high rate testing protocol in which the cells were both charged and discharged at the same high rates. As shown in Figure 3.6b, under this stringent condition, the 2D $LiFePO_4$/Ti thin film cathode can only store and deliver a capacity of 11 $\mu Ah/cm^2$ at 2C, or 20% of its capacity at 0.1C, while the 3D C/$LiFePO_4$/Ti/Ni nanoforests with the same $LiFePO_4$ mass loading can deliver as high as 152 $\mu Ah/cm^2$ at the same rate, or 84% of its capacity at 0.1C. Moreover, the nanoforest cathode with additional carbon coating can deliver 72% of capacity even at 10C, and 25% at 30C, respectively. This latter performance of 500

nm C-$LiFePO_4$ nanoforest cathode witnessed a significant improvement in rate performance over 30 nm $LiCoO_2$/Al nanorodes,[28] or 16 nm TiO_2/Ni nanorode electrodes.[29] The rate performance of our C-$LiFePO_4$ is slightly inferior to C-$LiFePO_4$ prepared by Martin's group using polycarbonate filter because the diameter of our C-$LiFePO_4$ is 10 times larger than Martin's C-$LiFePO_4$,[36] and kinetics of $LiFePO_4$ is very sensitive to particle size. With the same $LiFePO_4$ loading per footprint (1.06 mg/cm^2), the 3D C/$LiFePO_4$ forest electrodes provided more 15 times higher capacity than thin film electrode at 2C. The 3D C/$LiFePO_4$ forest cathode can even be charged and discharged at 30C, which is not capable for current thin film $LiFePO_4$ electrodes.

3.4.2 Electrochemical impedance spectroscopy (EIS)

To understand the origin of the superior rate performance of the TMV enabled $LiFePO_4$ nanoforest cathode, electrochemical impedance spectra (EIS) were carried out to analyze and compare the reaction resistances of the 3D nanoforest cathodes, both in absence and presence of carbon coatings, as well as the 2D thin film $LiFePO_4$ cathode. In all cases the working cathodes experienced 50 full cycles at 1C rate before being charged to 3.6V at 0.1C with a subsequent relaxation period of 2 hours.

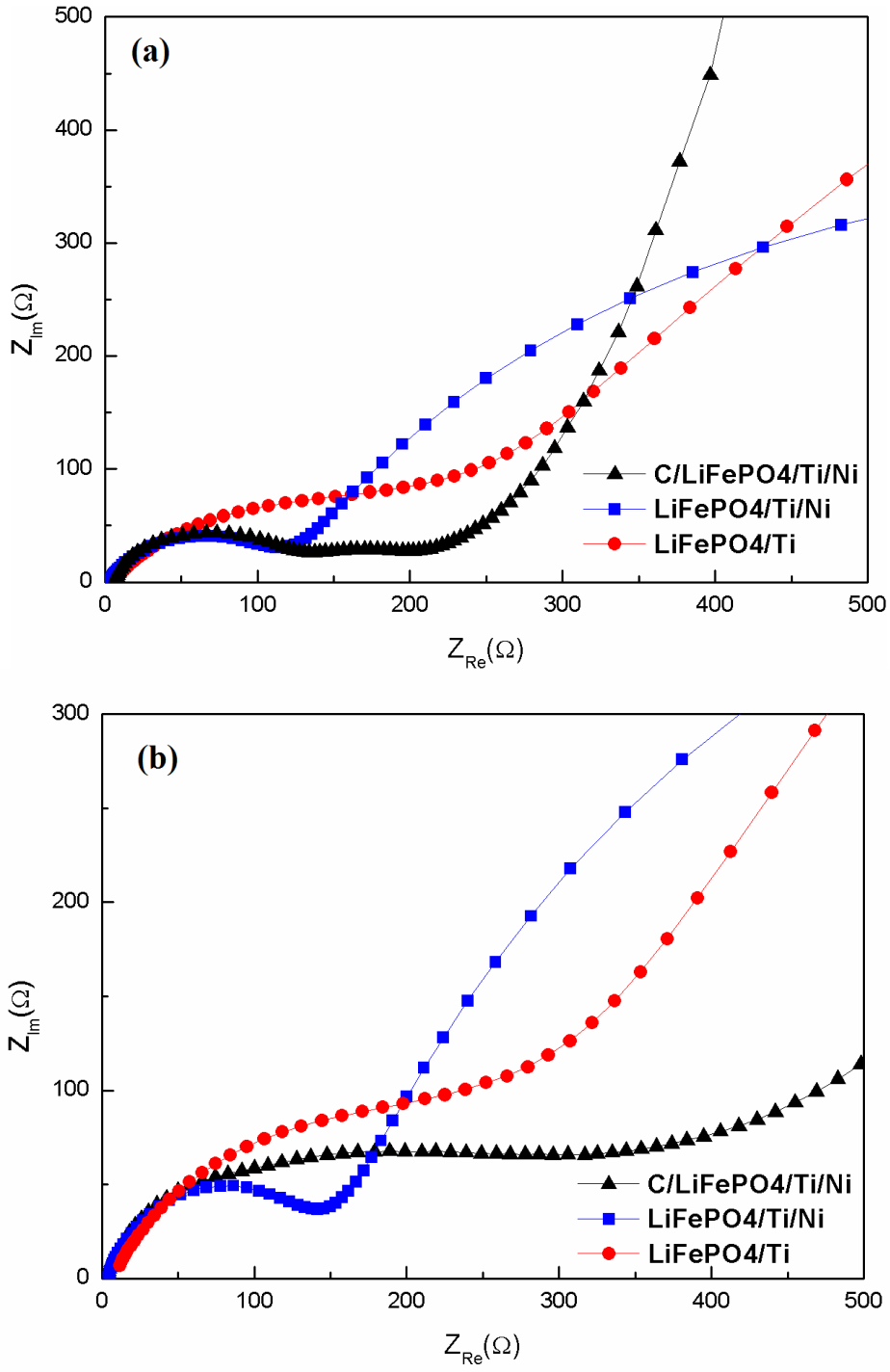

Figure 3.7 Typical Nyquist plots of three $LiFePO_4$ cathodes (a) after 50 charge/discharge cycles at 1C rate and (b) after 450 charge/discharge cycles at 1C rate, obtained after charging the $LiFePO_4$ cathode to 3.6 V and relaxation for 2 hours.

Figure 3.7a shows the Nyquist plots of three $LiFePO_4$ cathodes at 50^{th} charge/discharge cycle and Figure 3.7b is the Nyquist plots of three $LiFePO_4$ cathodes at 450^{th} cycle. For the fully activated $LiFePO_4$ electrodes (Figure 3.7a), the impedance spectra are typically composed of two partially overlapped semicircles in high and medium frequency regions, and a straight slopping line at low frequency.[47-52] The first semicircle at the high frequency region is attributed to the contact impedance between the current collector and the $LiFePO_4$ active materials, while the medium-frequency semicircle corresponds to the charge transfer impedance, which is largely overlapped by the low-frequency Li-ion diffusion line. The Ni nanorod core enhanced the contact between the current collector and the active species $LiFePO_4$ shell, reducing a contact impedance for the nanoforest cathode compared to that of the 2D $LiFePO_4$/Ti thin film cathode. The decreased $LiFePO_4$ thickness as well as low tortuosity paths for ionic transport from the liquid electrolyte into the $LiFePO_4$/Ti/Ni nanoforest cathodes also reduced the lithium-ion diffusion resistance, resulting in a short diffusion tail in low frequency and a short intersection in high frequency in the Nyquist plot, respectively. Further carbon coating on the $LiFePO_4$/Ti/Ni nanorods enhances the charge transfer resistance, reducing the size of the second semicircle and further shortening the low frequency tail, an indication that the C sub-layer also reduces the lithium-ion diffusion resistance in the $LiFePO_4$ in addition to its assistance in conducting electrons. The combination of these hierarchy elements synergistically leads to the observed superior rate performances of this nanoforest composite cathode.

3.4.3 Cycling stability

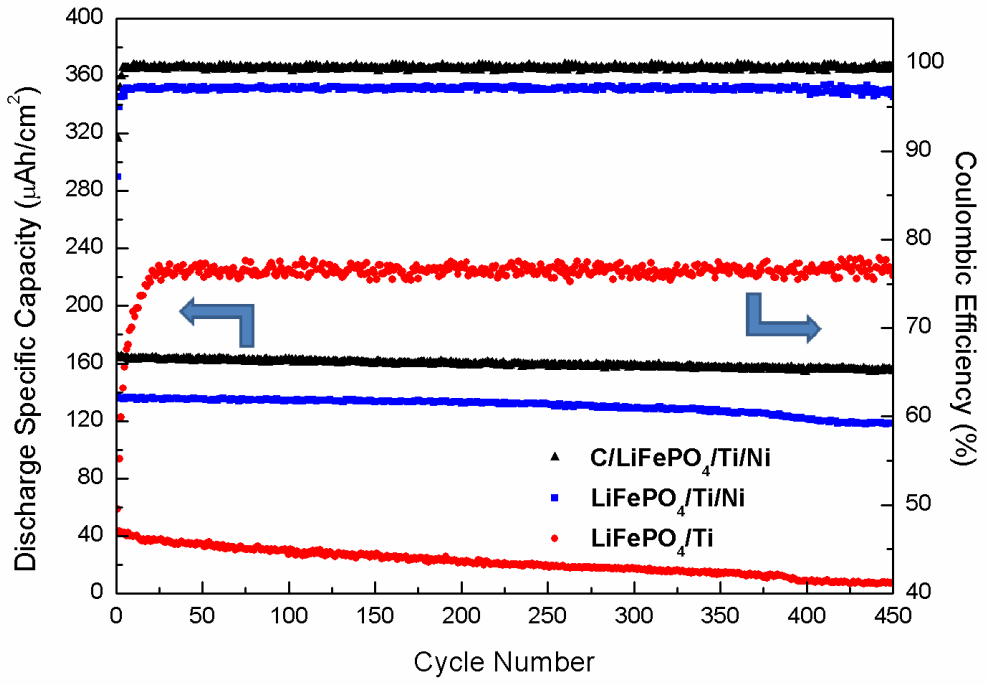

Figure 3.8 The cycling stability and Coulombic efficiency of $LiFePO_4$ cathodes at 1C charge/discharge current.

Finally, in addition to the enhanced reaction kinetics, the nanoforest cathodes also present much improved cycling stability. Figure 3.8 shows the cycling stability and Coulombic efficiency of two 3D nanoforest cathodes, C/$LiFePO_4$/Ti/Ni and $LiFePO_4$/Ti/Ni, with the 2D $LiFePO_4$ thin film cathode as comparison. The 3D C/$LiFePO_4$/Ti/Ni nanoforest cathode only decays 0.014% per cycle during cycling at a rate of 1C for 450 cycles, while the corresponding Coulombic efficiency quickly rises to ~100% after the first 5 cycles. The 3D nanoforest sample without C sub-layer

shows a similar cycling stability but with a slightly lower Coulombic efficiency in the first 350 cycles and observable capacity fading thereafter. As comparison, the 2D $LiFePO_4$/Ti thin film cathode without any of the hierarchical nano-architecture shows more than a 10 times faster capacity decay and low Coulombic efficiency. The low Coulombic efficiency of $LiFePO_4$ thin film electrode in the first few charge/discharge cycles has been reported.[53,54] The irreversible capacity loss in the first few cycles was attributed to the oxidation of surface impurities such as $Li_xFe_yO_z$, resulting in partial deintegration of iron oxide and ion dissolution into electrolyte. Since the electrochemical oxidation of $Li_xFe_yO_z$ is not reversible, it decreases the Coulombic efficiency. Carbon coating can suppress the iron dissolution into electrolyte which enhances the Coulombic efficiency.

As discussed previously, the remarkable cyclic stability of the TMV enabled $LiFePO_4$ nanowire forest cathode could come from the unique multi-layer nano-hierarchy of the cathode. Specifically, the highly robust and conductive Ni sub-layer strongly binds with active $LiFePO_4$ sub-layer through a Ti sub-layer and directly connects to the main substrate to form a 3D nanowire extending deeply into the high aspect ratio nanorods. As shown via SEM (Figure 3.2d) and TEM (Figure 3.4g) small particles appeared on the surface of the $LiFePO_4$ nanorods but still bonded to the nanorods even after 450 charge/discharge cycles. The carbon coating further improved the morphology and structural stability of 3D $LiFePO_4$ nanoforest cathode. For C/$LiFePO_4$/Ti/Ni nanoforest sample, the surface remains smooth (Figure 3.2f) after 450 cycles although part of the carbon coating layer is detached from $LiFePO_4$

shell (Figure 3.4j). These findings indicate that the carbon coating help in stabilizing the surface morphology of the $LiFePO_4$ layer.

The structural degradation of the $LiFePO_4$ cathodes during charge/discharge cycles would also decrease the kinetics of lithiation/de-lithiation as demonstrated by EIS (Figure 3.7b). Comparing EIS at the 50^{th} and 450^{th} cycle in Figure 3.5, the impedance of all three $LiFePO_4$ cathodes increased with charge/discharge cycles. Both contact impedance (the first semicircle) and charge transfer impedance (the second semicircle) are enlarged after 450 charging/discharging cycles, suggesting the phase transformation generated stress/strains that weakened the bonding between the sub-layers of the metal conductor and the active $LiFePO_4$. Phase transformation also induces a change in the morphology of the carbon coating, which increases the charge transfer resistance. The increase in contact resistance and charge transfer resistance in the C/$LiFePO_4$/Ti/Ni nanoforest cathode cause the two semicircles at 50 cycles to merge into a larger one. Thus this hierarchical nano-architecture with core-shell arrangements allows the electrode to be charged and discharged at high C-rates with minimized electrochemical and mechanical stresses, resulting in a significant cycling stability improvement over previously reported $LiFePO_4$ nanowire-based cathodes.

It must be pointed out that, while a fully mature application of the process requires both anode and cathode to be architectured in a complementary manner, so that their respective 3D configurations could match each other to make a full battery, we have in our previous work architectured a high capacity 3D anode materials based on Si-Li alloy. Undoubtedly integrating these two electrochemical couples would

need further work, but we believe that the current work on 3D $LiFePO_4$ makes one step progress toward that destination.

3.5 Summary

In summary, an IC-friendly process using genetically-modified TMV as "bottom-up" templates leads to $LiFePO_4$-based nanoforest cathode arrays with multi-layered hierarchy that functions synergistically to store and deliver energy in small footprint at excellent efficiency and stability. Within the TMV-enabled dense nanoforest cathodes, both ionic and electronic migration lengths are significantly reduced while the mechanical and electrochemical stresses between the intercalation host ($LiFePO_4$) and main current collector are also minimized. The vertical alignment of $LiFePO_4$ nanoforest on SS current collector, enabled by the genetic modification of TMV, and the facile multiple sputtering deposition process provide a valuable new avenue to the 3D electrode array design and architecturing. In particular, the built-in metallic nano-current collector, which significantly enhances the connection between the active sub-layer and the main current collector, might provide a versatile solution to the common "electron transfer" issues of high aspect ratio nano-structures.

Chapter 4: Tin Coated Virus Nanoforests for Sodium-Ion Battery Anodes

4.1 Introduction

Since its commercialization two decades ago, Li-ion batteries have essentially dominated the portable electronics applications in small formats while being poised to enter more profitable and strategically important markets of automotive and grid storage. However, the limited abundance of Li in earth-crust, its uneven geographic distribution and difficulties in recycling Li resources have raised concerns about large scale application of this chemistry. As alternative to Li-ion chemistry, Na-ion batteries have attracted increasing attention, both because of the low cost associated with its high natural occurrences in both earth and ocean, and decent energy densities blessed by its similar chemical natures to Li. Given this similarity, many mature electrode materials for Li-ion chemistry have been investigated as drop-in replacement for Na-ion; however, most of the efforts were rendered ineffective, as evidenced by the low capacities utilization, inferior rate capability, poor cycling stability or even complete electrochemical inactivity, for which the larger size of Na-ion relative to Li-ion is generally believed to be responsible.[55,56] More specifically, although a few cathode candidates borrowed from Li-ion chemistry do intercalate/de-intercalate Na-ion reversibly,[57-72] the availability of such anode materials is much rare. It has been reported that carbonaceous materials,[73-77] TiO_2,[78] Sb_2O_4,[79] Sb,[80] SnSb,[81] and Sn[82-84] can store/release Na-ion with decent reversibility,

among which Sb/C composite seems to provide the best performance of 575 mAh g^{-1} over 100 cycles.[80]

Despite the high theoretical capacity of Sn (847 mAh g^{-1} corresponding to $Na_{15}Sn_4$), the much larger volume expansion of Sn (520%) than Sb (390%) during sodiation essentially prevents the access of this capacity.[82,84] This effect of volume change has been familiar for Si or Sn as lithiation hosts, and larger size of Na-ion significantly worsened it. In addition to this complication, Sn particles also tends to aggregate into large particles and then pulverize to isolate from electrode during the electrochemical alloying/de-alloying, which further disrupts the electrode integrity and leads to rapid deterioration in cycling stability.[85] Mainly because of these two failure mechanisms, the best cycle life reported for nano-Sn was represented by only less than 25 charge/discharge cycles for Na-ion storage.[82,84] To circumvent these issues, Xiao *et al*. developed nano-sized binary elemental alloys such as SnSb/C to reduce stress/strain and to dilute the opportunities of Sn aggregation, which achieved a unprecedented capacity of 435 mAh g^{-1} over 50 cycles.[81]

In this work, we adopted two separate strategies to address the issues of pulverization and aggregation of Sn-based anodes. First, we introduced nano-hierarchy into Sn electrodes by depositing Sn nanoparticles on Ni coated *Tobacco mosaic virus* (TMV), which was genetically modified to express 100% cystein (Cys) on its major coat protein. Virus has been successfully used as bio-inorganic template to synthesize electrode materials for rechargeable batteries[39] and TMV1cys has been demonstrated as a versatile template for 3D nanoforest electrodes of a number of different chemistries.[86] Using the known three-dimensional structure of TMV a

novel virus mutant, TMV1cys, was created by inserting a cysteine codon within the N-terminus of the coat protein open reading frame.[33,34] The positioning of the 1cys thiol group contributes to the attachment and vertical positioning of the viral rods onto metal surfaces. Although surface exposed, the 1cys residue is recessed within a groove and partially covered by the C-terminal arm of the coat protein. This position likely inhibits direct contact between the cysteine derived thiol and a surface except at the 3' end of the virus rod where the thiol group is sufficiently exposed to make direct surface contact, which leads to 3D electrode arrays in nearly vertical manner (Figure 4.1).

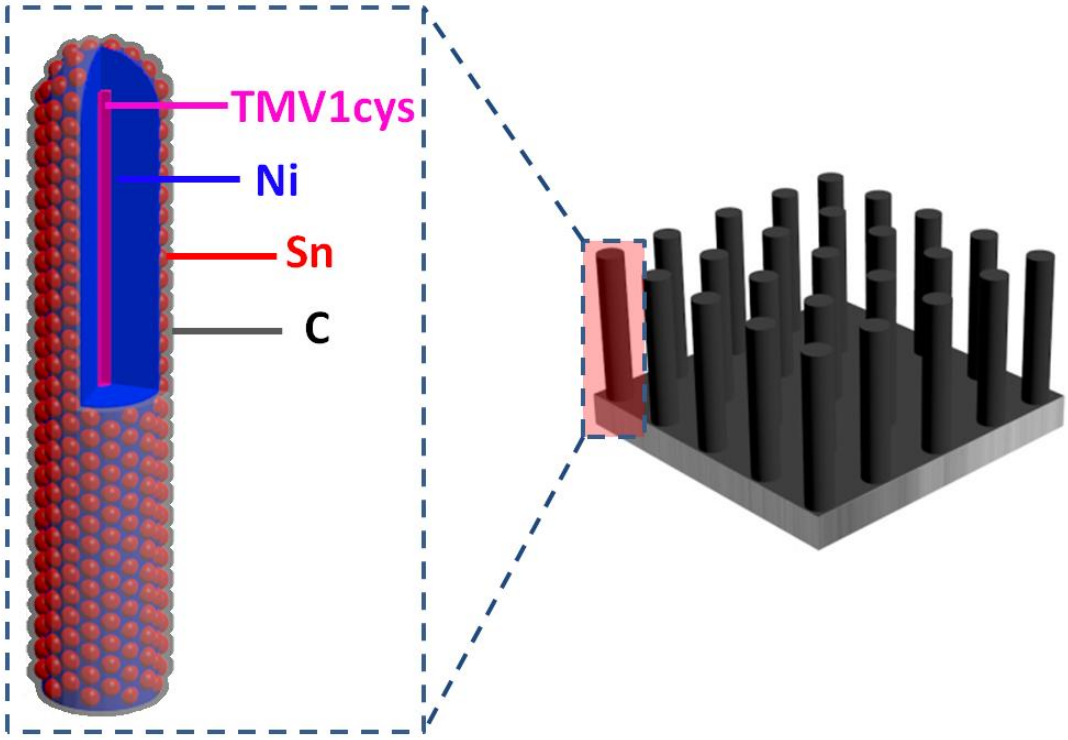

Figure 4.1 Schematic illustration of the 3D C/Sn/Ni/TMV1cys anode arrays and the cross-section of hierarchical structure of a single Sn nanorod.

After Sn nanoparticles were deposited over Ni-interlayer formed by electroless plating, the buffering spaces between each individual nanorods would effectively accommodate the volume expansion of Sn while still maintaining high capacity loading per footprint. Secondly, a thin-layer of carbon was coated over the active Sn sublayer, suppressing possible aggregation during the electrochemical reactions by diminishing the diffusion of Sn (Figure 4.1).

With this hierarchy consist of multiple functional layers on nanoscale, we anticipated that the stress caused by the large volume change of Sn would be effectively alleviated,[87,88] and highly conductive pathway for electrons would be established by the Ni-sublayer between the Sn and current collector. It was also known that Ni nanorods can alloy with Sn, which would enhance the robustness of Sn particles through intermetallic bonding potentially.[89-95] Additional coating of carbon sublayer over Sn should suppress aggregation and pulverization of Sn, further improving electrochemical performance.[96-100]

4.2 3D C/Sn/Ni/TMV1cys nanoforest anode preparation

Thus, the Sn nanoforest anode was fabricated on the Ni/TMV1cys assemblies that are vertically aligned on stainless steel (SS) current collector. A ~50 nm nickel (Ni) was first deposited on TMV1cys nanorods in an electroless plating bath to form a longitudinal electron pathway along the inner core of each nanorods. A rough layer (20 nm) of Sn and 5 nm layer of carbon were then sequentially placed onto Ni-sublayer using physical vapor deposition (PVD) and radio-frequency (RF) magnetron sputtering deposition, leading to the configuration of C/Sn/Ni/TMV1cys.

The Sn layer was deposited on stainless steel (SS) discs (15.5mm in diameter) containing preassembled Ni coated TMV1cys templates by physical vapor deposition (PVD) under continuous vacuum. The SS discs were polished carefully and cleaned by sonication in alcohol and acetone before loading into the vacuum chamber. The patterned 3-D TMV1cys templates and Ni coating were done as previously described.[31] A Sn pellet (99.999%, Kurt J. Lesker Company) was used as Sn source for PVD. In order to get a uniform morphology, the Sn deposition rate was kept as low as 0.02 nm s^{-1}. The carbon sputtering was conducted in an Ar atmosphere (1 Pa) using a DC power density of 4.5 W/cm^2. The target-to-substrate separation was 11 cm. In comparison, Sn/SS thin film anode with a 20nm thickness was also prepared under the same PVD conditions and the thickness was confirmed by the film thickness monitor of the Metra Thermal Evaporator.

4.3 Characterization of 3D C/Sn/Ni/TMV1cys nanoforest anode

The Sn loading mass of each sample was measured by high-precision microbalance (Mettler Toledo, XS105 dualRange) within an accuracy of 1 μg. Raman scattering spectrum were collected by Horiba JobinYvonLabRAM Raman microscopes (models ARAMIS) with 633nm excitation line. The surface morphology of the samples was characterized by scanning electron microscopy (HITACHI SU-70). A high-resolution transmission electron microscopy (HRTEM, JOEL JEM 2100F) with an energy-dispersive spectrometer (EDS) was employed to analyze the microstructures and interface characteristics of the film stacks.

4.3.1 SEM, TEM and EDS line scan profile

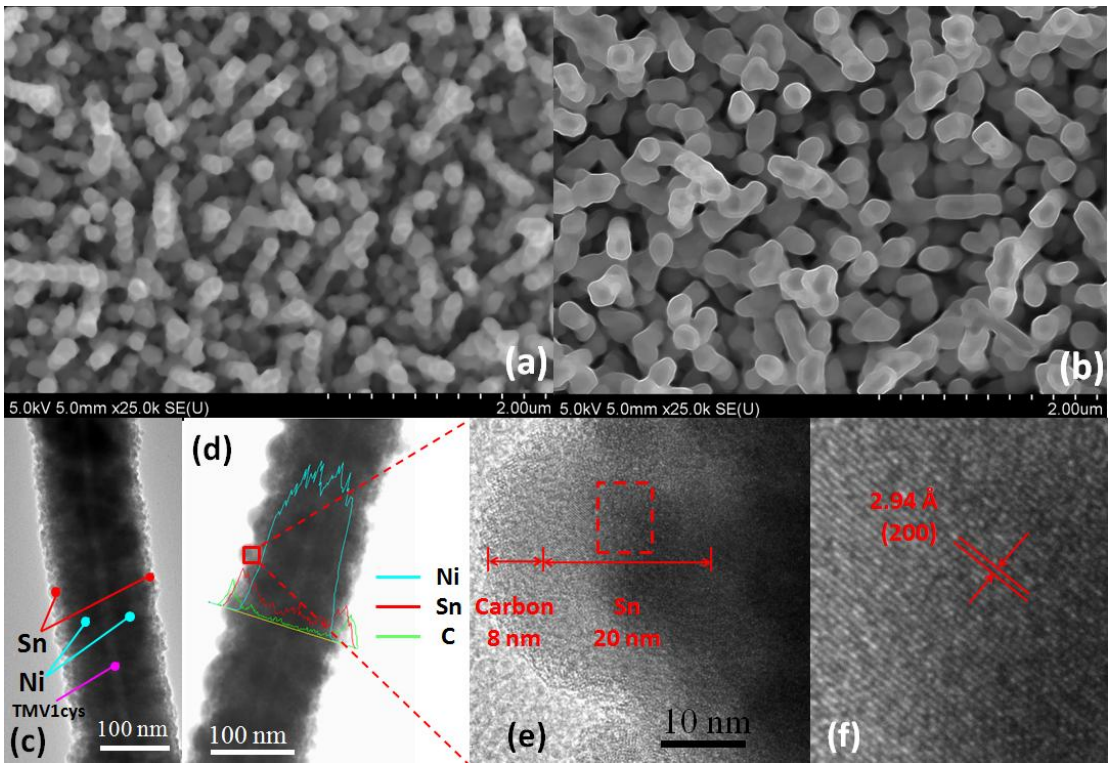

Figure 4.2 SEM images of (a, b) as-deposited 3D Sn/Ni/TMV1cys and 3D C/Sn/Ni/TMV1cys anodes. TEM images of (c) a single C/Sn/Ni/TMV1cys nanorod, and its the EDS line scan mapping profile (d), (e) high-resolution TEM image of the Sn crystal and the amorphous outer-layer, and (f) enlarged high-resolution TEM image of the Sn crystal of the red rectangle area in (e).

Figure 4.2a-b show the SEM images of near-vertical assembly of Ni/TMV, Sn/Ni/TMV and C/Sn/Ni/TMV on SS current collector, respectively. As a reference for comparison, 2D Sn thin film with 20 nm thickness was also directly deposited on SS substrate under the same conditions. The hierarchy, structure and configuration of virus-templated C/Sn nanorods were further confirmed by transmission electron microscopy (TEM) and energy dispersive spectroscopy (EDS). Figure 4.2c-f show the

TEM images of single Sn/Ni/TMV1cys and C/Sn/Ni/TMV1cys nanorod, and the EDS line scan mapping profile with the high-resolution images. In Figure 4.2c, a thin layer of Sn was clearly visible with thickness of ~20 nm, whose loading is ~ 0.8 mg (0.5 mg cm^{-2}) in mass. The loading mass of Sn was obtained by weighting the mass difference before and after Sn physical vapor deposition using high-precision microbalance (Mettler Toledo, XS105 dualRange) within an accuracy of 1 μg. The EDS line scan mapping demonstrated the layer structure and confirmed the SEM images shown in Figure 4.2b. Both SEM and TEM images cooperatively revealed that all the nanorods have Ni/TMV1cys core that directly mounted on the SS main current collector, providing a longitudinal current collector sublayer. This metallic nanotube has been proven effective in resolving issues associated with electron-transfer kinetics along the high aspect-ratio nanorod-/nanowire-like materials, for which nanoscale intimacy between all functional sublayers has been a challenge.

It should be note that after carbon coating, the Sn-sublayer structure anchored on the Ni nano-shell changed from smooth thin film (Figure 4.2c) to a more particulated shape (Figure 4.2d), indicating that Sn thin layer may have aggregated into nanoparticles during RF carbon sputtering deposition process. The high resolution TEM image (Figure 4.2e and 4.2f) shows a core-shell configuration for these C/Sn particles, with crystalline core and amorphous shell layer, a 2.94 angstroms interplanar space can be assigned to the (200) plane of Sn in Figure 4.2f. From the EDS line scan mapping in Figure 4.2d and TEM in Figure 4.2e, the thickness of carbon layer on the surface of the Ni nanorods is ~5 nm.

4.3.2 Raman spectra

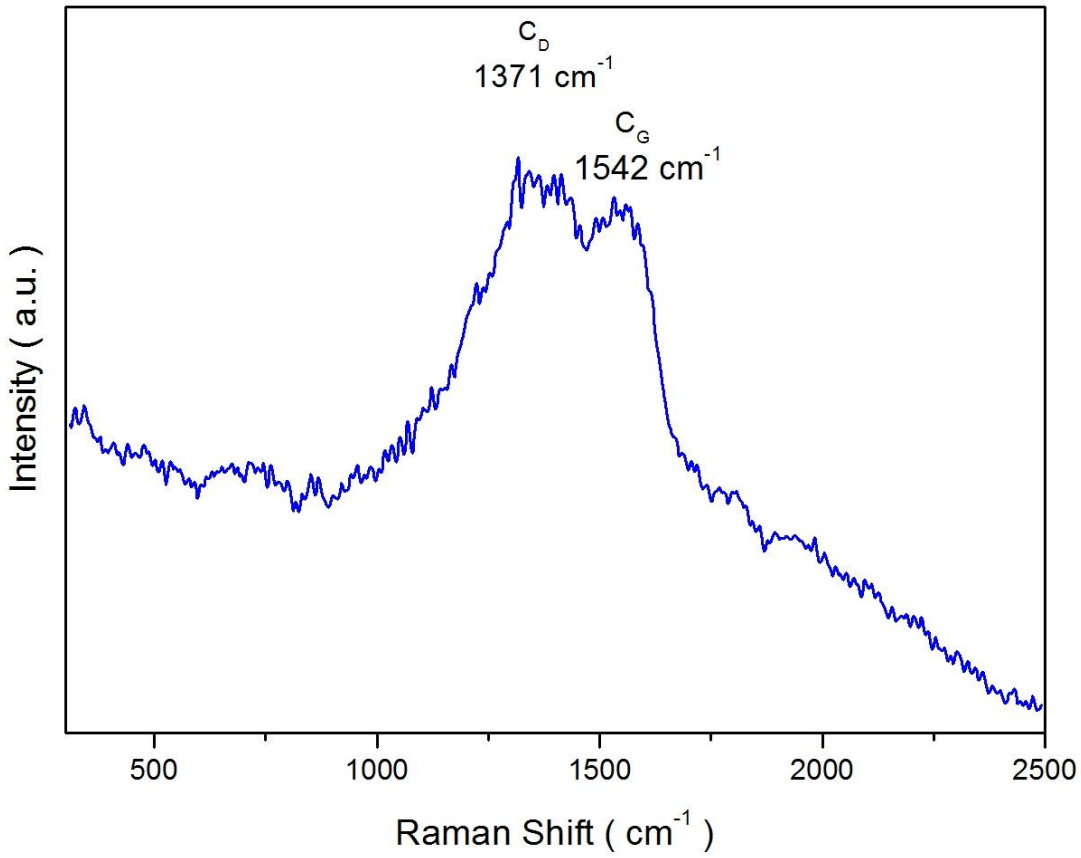

Figure 4.3 Raman spectra of 3D C/Sn/Ni/TMV1cys nanoforest anode.

The graphitization degree of the carbon layer was investigated using Raman spectrum (Figure 4.3), showing two bands of D and G at 1371 and 1542 cm^{-1}, respectively, in accordance with disorder and graphitic crystal features of carbon.[43] The stronger D band suggests that the carbon layer on the C/Sn/Ni/TMV1cys nanorods has low crystallinity, typical of disordered carbonaceous material.

Summarizing the images and chemical analyses, the composite electrode array templated on virus-carry nearly-uniform Sn active sublayers in a multi-layered nano-hierarchy, wherein primary Sn nanoparticles reside on a secondary nanorods vertically standing on current collector, while additional inert ingredients exist

between active materials and current collector as functional sublayers. The overall electrochemical performance should be improved due to the array's spatial tolerance against accommodate volume change, its mechanical robustness to maintain material integrity, its high electron conductivity in longitudinal direction, and its 3D architecture to store Na-ion vertically above the main current collector.

4.4 Electrochemical tests result and discussion

Electrochemical performance of the Sn anodes were tested in coin cells (R2032) using Sodium metal as counter electrode and 1 M $NaClO_4$ solution in ethylene carbonate/diethyl carbonate (EC/DEC, 1:1 by vol. %) as electrolyte. The charge/discharge testing was carried using an Arbin BT-2000 battery test station over the voltage range of 0.05-1.5V versus Na/Na^+. The Cyclic Voltammetry (CV) curves were collected using a Solartron 1260/1287 with a scan rate of 0.1 mV s^{-1} and a scan range from 0 V to 2 V for 5 cycles. All electrochemical experiments were conducted at room temperature and all capacity values were calculated based on the weight of Sn.

4.4.1 Cyclic voltammetry

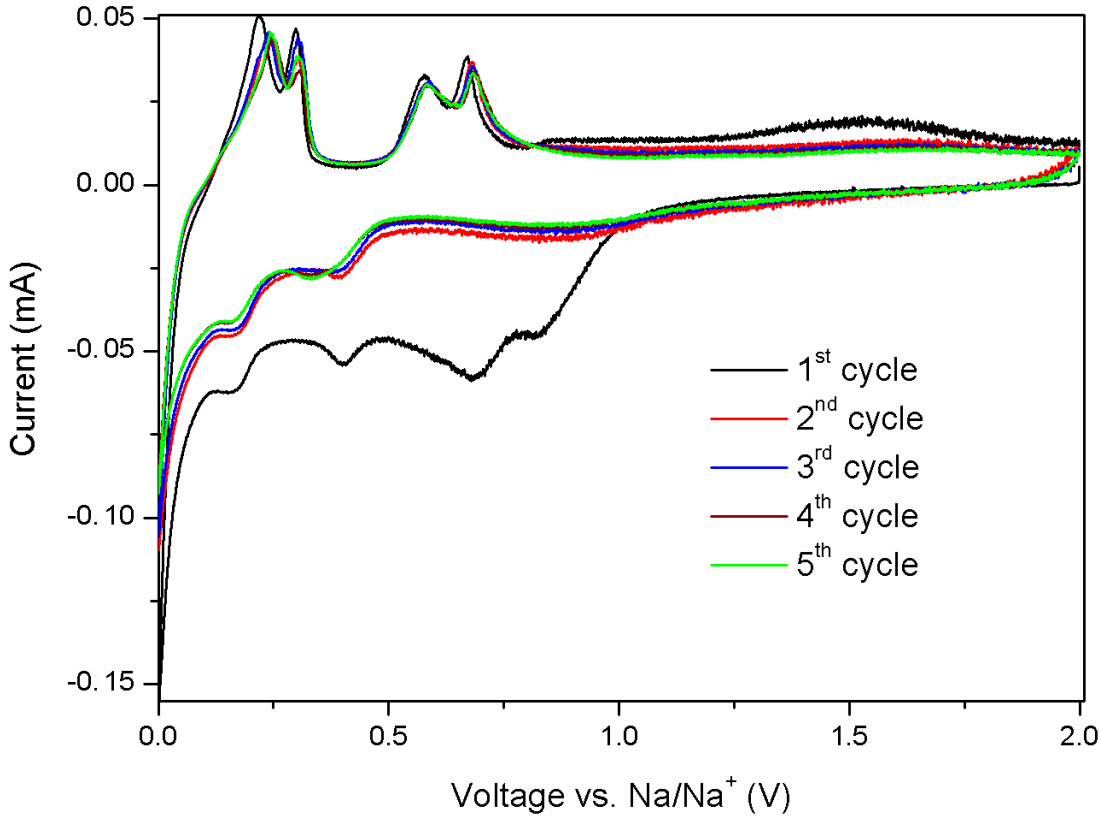

Figure 4.4 Cyclic voltammetry of C/Sn/Ni/TMV1cys nanoforest anode with a scan rate of 0.1 mV s^{-1} between 0.0 and 2.0 V.

The sodiation and de-sodiation of C/Sn/Ni/TMV nanoforest anodes was characterized using cyclic voltammetry (CV). As shown in Figure 4.4, five peaks, located at 0.82, 0.68, 0.40, 0.15 and 0.0V respectively, were observed in the first sodiation process. Because the two sodiation peaks at higher voltage disappeared in the subsequent cycles, they were possibly attributed to the formation of solid electrolyte interphase (SEI) film caused by the decomposition of electrolyte, which contributes to the irreversible capacity. The de-sodiation process presents four well-defined peaks at 0.22, 0.30, 0.58 and 0.67 V, which are attributed to the alloy

compounds of $Na_{15}Sn_4$, Na_9Sn_4, NaSn, $NaSn_5$, respectively, with a two-phase reaction mechanism.[83] All these de-sodiation potentials are in good agreement with the calculated and experimental results of Sn reported previously.[82-84] Ni (or potential NiO) core in C/Sn/Ni/TMV anodes turned out to be inactive for Na.[82] The contribution in capacity from carbon coating can be neglected due to the low presence of carbon in the composite material (C/Sn= 7 wt%). The unchanged peak current intensity implies excellent reversibility of the C/Sn/Ni/TMV1cys nanoforest anode.

4.4.2 Cycling stability

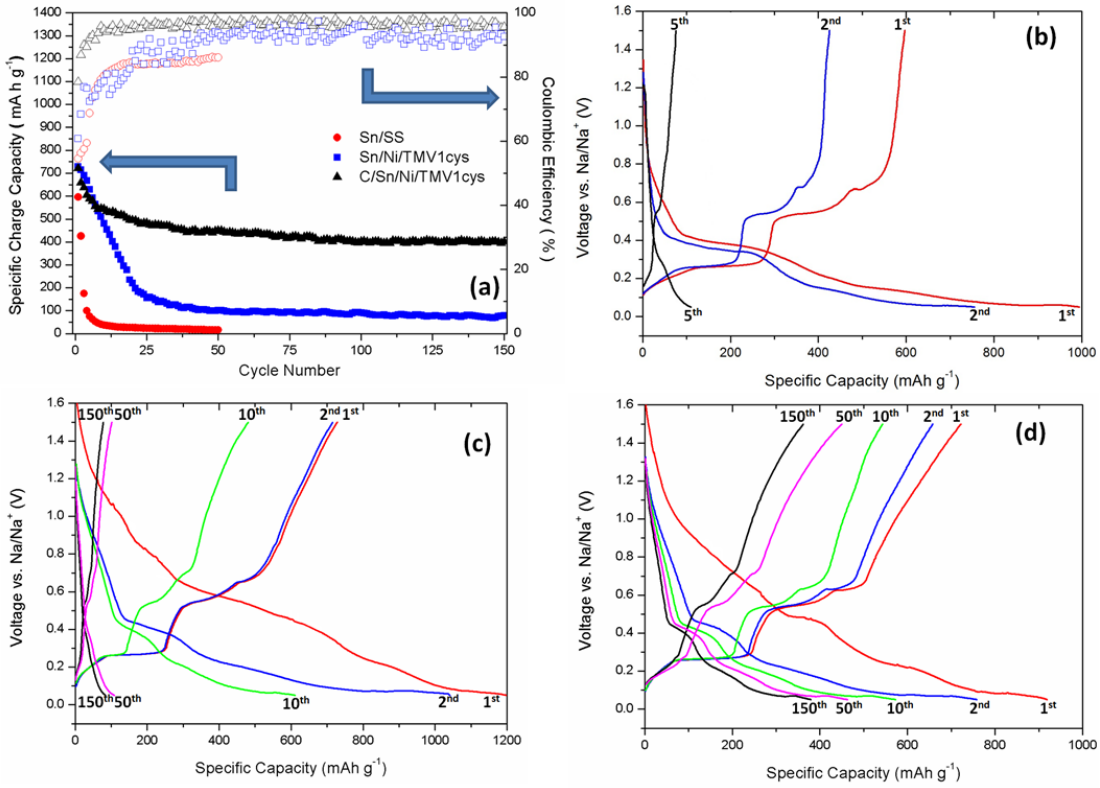

Figure 4.5 (a) Cycling performance of 2D Sn thin film, 3D Sn/Ni/TMV1cys, and 3D C/Sn/Ni/TMV1cys anodes, and sodiation/de-sodiation voltage profiles of (b) 2D Sn thin film, (c) 3D Sn/Ni/TMV1cys, and (d) 3D C/Sn/Ni/TMV1cys nanoforest anodes, at current density of 50 mA g^{-1}.

The cycling performance of 3D Sn/Ni/TMV1cys and 3D C/Sn/Ni/TMV1cys anodes was investigated by galvanostatic charge and discharge of the electrodes between 0.05 and 1.5 V at the current density of 50 mA g^{-1} (Figure 4.5a), with 2D Sn thin film (with the same thickness of 20nm as 3D nanoforest Sn anode) as reference for comparison. All three Sn anodes provided around 730 mAh g^{-1} at the first de-sodiation process, which is close to the theoretical capacity (847 mAh g^{-1})

corresponding to $Na_{15}Sn_4$, approximately three times larger than that of hard-carbon. The capacity of 2D Sn thin film anode suffered a rapid capacity fading, retaining only 9% of the initial capacity within 5 cycles. In contrast, the Sn/Ni/TMV1cys nanoforest anode maintains 30% of initial capacity after 20 cycles, which is a visible improvement over that of reference. After 40 cycles, its capacity stabilized at ~100 mAh g^{-1}. The cycling stability was significantly extended by a thin layer (5 nm) carbon coating on Sn/Ni/TMV1cys nanoforest: after slight decrease in the initial few cycles, the capacity stabilized around 405 mAh g^{-1} after 150 cycles, corresponding to retention of 55%, which is much higher than those without carbon coating, demonstrating that carbon coating can effectively suppress the Sn aggregation.

Aside from capacity, voltage profiles actually reveal more details about the electrochemistry of sodiation/de-sodiation in a Sn host. These voltage profiles of 2D Sn thin film, 3D Sn/Ni/TMV1cys and 3D C/Sn/Ni/TMV1cys anodes are depicted in Figure 4.5b-d, respectively, with cycle numbers labeled on individual curves. The step potential plateaus between 0.0 and 0.7V were presented in the first de-sodiation for all three kinds of anodes, which is characteristic of de-alloying $Na_{15}Sn_4$. This is consistent with the CV curves in Figure 4.4. As shown in Figure 4.5b, the capacity in each potential plateau of 2D Sn thin film anodes rapidly decreased with cycling, suggesting that Sn film disintegrating and detaching electronically from current collector. In contrast, the step potential plateaus of 3D Sn/Ni/TMV1cys anodes remained visible even after 10 cycles, but eventually disappeared after 150 cycles (Figure 4.5c), indicating that the nano-structure of Sn/Ni/TMV helped but was still not robust enough to withstand the volume change and aggregation in extended

charge/discharge cycles. However, the thin layer carbon coating made much more pronounced difference, maintaining these distinct step-plateaus even after 150 full charge/discharge cycles (Figure 4.5d).

4.4.3 After cycling SEM and TEM

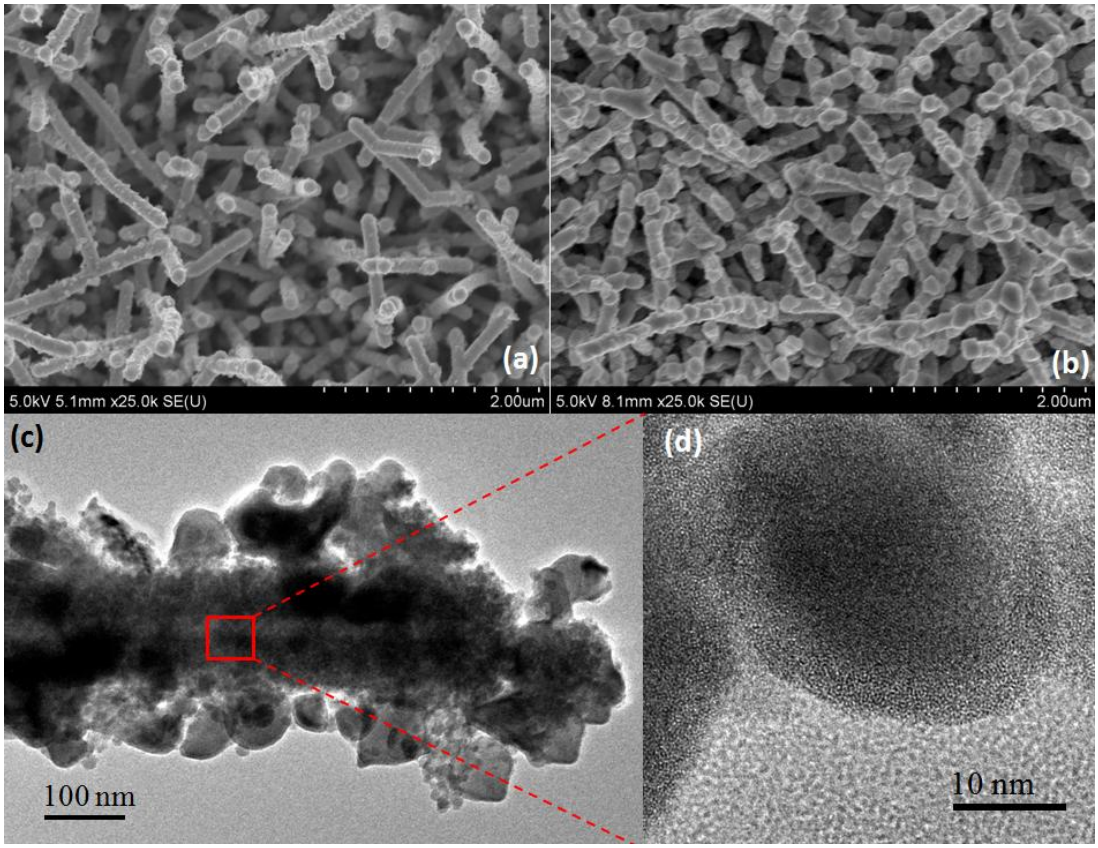

Figure 4.6 SEM images of (a) 3D Sn/Ni/TMV1cys anode and (b) 3D C/Sn/Ni/TMV1cys anode after 150 charge/discharge cycles at current density of 50mA g^{-1}. (c) TEM image of a single C/Sn/Ni/TMV1cys nanorod after 150 charge/discharge cycles at current density of 50mA g^{-1}, (d) enlarged high-resolution TEM image of the after-cycling amorphous Sn.

To gain insight into the capacity fading mechanism and any accompanying structural change of these anodes during cycling, SEM and TEM images were collected from 2D Sn thin film anode after 50 cycles, 3D Sn/Ni/TMV1cys and 3D C/Sn/Ni/TMV1cys anodes after 150 cycles (Figure 4.6). Sn nanoparticles in 2D thin film apparently coalesced into large particles and pulverized, and most Sn peeled off from the current collector, leading to severe capacity fading. In 3D Sn/Ni/TMV1cys anodes, although some of Sn still remained on Ni/TMV1cys nanorods after 150 cycles (Figure 4.6a) thanks to the nano-structure, the cleaner surfaces of Sn/Ni/TMV nanorodes suggested that the majority of Sn particles detached from the Ni nanorode current collectors. The reason is probably the same as the 2D Sn thin film anode where the Sn particles tend to aggregate to from larger particles during sodiation/de-sodiation processes, a process likely driven by the thermodynamics of intermetallic alloy compounds. Once the Sn particles grew to certain size, they pulverized and lost contact with current collectors, thus becoming electrochemically inactive.

On the other hand, the after-cycling SEM image of C/Sn/Ni/TMV1cys (Figure 4.6b) clearly shows that the most of the Sn-sublayer still remained on the nano current collectors even after 150 cycles, and the growth of Sn particle size is apparently suppressed (Figure 4.6c), most likely due to the protection effects of carbon coating. This validates our hypothesis that Sn aggregation during electrochemical extended sodiation/de-sodiation cycles could be mitigated by carbon coating, based on earlier experience that carbon has been effective in suppressing Sn aggregation during lithiation/de-lithiation.[96-100] The C/Sn/Ni/TMV1cys sample obtains the best stability among the 3 electrodes, not only because of the 3D nano-

structure enabled by viral templates, but also because the carbon coating physically separates the crystal particles and relieves the aggregation between the Sn particles.

4.5 Summary

In summary, 3D Sn nanoforest anode arrays consisting of individual nanorods, whose multiple functional layers include a carbon outer-shell, a Sn intermediate-layer and a metal inner-core, were fabricated by PVD, RF magnetron sputtering and electroless deposition on patterned TMV1cys templates. The C/Sn/Ni/TMV1cys nanorods with 0 nm thickness of Sn demonstrated superior electrochemical performances toward Na-ion storage and release. The vertical alignment of nanorods as well as the precise hierarchical control of various sublayers of materials in designed order were believed to function synergistically to maintain an alloy anode host mechanically, electronically and electrochemically stable, despite its >500% volume change upon sodiation/de-sodiation cycles. In particular, the carbon coating on the Sn particles minimized the Sn particle aggregation, which has been a rather severe challenge that this high capacity alloy host is facing. The resultant C/Sn/Ni/TMV1cys nanorods can provide 722 mAh g^{-1} capacity toward Na-ion in the initial cycles and retain 405 mAh g^{-1} after 150 cycles, demonstrating the longest-cycling nano-Sn anode material for Na-ion batteries reported in literatures to date. The superior cycling performance, combined with the simplicity of the TMV1cys self-assembly and patterning process, represents a new strategy for the development of inexpensive and versatile synthesis techniques for Na-based energy-storage applications.

Chapter 5: Conclusion and future work

5.1 Conclusion

The first work, C/$LiFePO_4$/Ti/Ni/TMV1cys nanoforest cathode, enables an elegant bottom-up solution to engineer 3D micro-battery arrays as integral power sources for micro-electronics. Thus, multilayers of functional materials were hierarchically architectured over Tobacco mosaic virus (TMV) templates that were genetically-modified to self-assemble in a vertical manner on current-collectors, so that optimum power and energy densities accompanied with excellent cycle-life could be achieved on a minimum footprint. The resultant micro-battery based on self-aligned $LiFePO_4$ nanoforests of shell-core-shell structure, with precise arrangement of various auxiliary material layers including a central nanometric metal core as direct electronic pathway to current collector, delivers excellent energy density and stable cycling stability only rivaled by the best Li-ion batteries of conventional configurations, while providing rate performance per foot-print and on-site manufacturability unavailable from the latter. Carbon coated $LiFePO_4$/Ti/Ni nanoforests enhanced the capacity of active species 162 $\mu Ah/cm^2$, and it only decays 0.014% per cycle during cycling at a rate of 1C for 450 cycles

The C/Sn/Ni/TMV1cys nanoforest anode, designed as high capacity alloy host for Na-ion chemistry, forest of Sn nanorods with a unique core-shell structure were synthesized on viral scaffolds, which were genetically engineered to ensure a nearly vertical alignment upon self-assembling onto metal substrate. The interdigital spaces thus formed between individual rods effectively accommodated the volume

expansion and contraction of the alloy upon sodiation/de-sodiation, while additional carbon coating engineered over these nanorods further suppressed Sn-aggregation during extended electrochemical cycling. Due to the unique nano-hierarchy of multiple functional layers, the resultant 3D nanoforest of C/Sn/Ni/TMV1cys, binder-free composite electrode already and evenly assembled on stainless steel current collector, exhibited supreme capacity utilization and cycling stability toward Na-ion storage and release. An initial capacity of 722 mAh $(g\ Sn)^{-1}$ along with 405 mAh $(g\ Sn)^{-1}$ retained after 150 deep cycles demonstrates the longest-cycling nano-Sn anode material for Na-ion batteries reported in literatures to date and marks a significant performance improvements for neat Sn material as alloy host for Na-ion chemistry.

Both approaches could open a new avenue for micro-electromechanical systems (MEMS) applications, which would significantly benefit from the concept that electrochemically active components be directly engineered and fabricated as an integral part of the integrated circuit (IC).

5.2 Future work

Although the microbattery electrodes have obtained excellent energy density and cycling stability, it is still far away from commercialization. The most simple and practical part of future work can be the full battery assembling using $C/LiFePO_4$/Ti/Ni/TMV1cys nanoforest cathode and Si/Ni/TMV1cys nanoforest anode.

The safety of microbatteries also should be concerned in the future work. The high reactivity of lithium restricts its use as anode in real batteries, and rechargeable lithium batteries failed to be introduced into the market due to safety concerns. Due to

the low potential of the lithium deposition, it is possible that large amount dendrites will grow on the anode side during cycling. And the sharp dendrites can penetrate the polymer membrane separator easily to cause short circuit. At the same time. the overcharge or overdischarge of the batteries can also lead to the decomposition of the liquid electrolyte. In these extreme situations, both short circuit and electrolyte decomposition can cause explosion with flame. Thus, a careful control of the charge procedure is needed to avoid major accidents.

The all-solid-state microbattery could be the most feasible solution to the safety problem. The use of true solid electrolyte with no added liquid solvent and no significant vapour pressure would make the battery suitable to special design and unusual applications. Deposition techniques exploited in the previous work should be suitable to fabricate 3D Si/LiPON/C/$LiFePO_4$/Ti/Ni/TMV1cys or $NaMn_2O_4$/NaPON/Sn/Ni/TMV1cys all-solid-state microbatteries. Since the virus enabled 3D electrodes have been well developed in previous chapters, we have enough confidence to expect that the all-solid-state microbattery based on the virus enabled 3D current collector can not only avoid catching fires in extreme situations but also acquire extremely high energy density and cycling stability.

Bibliography

1. V. Etacheri, R. Marom, R. Elazari, G. Salitra, D. Aurbach, *Energy Environ. Sci.*, **2011**, 4, 3243-3262
2. http://www.nexeon.co.uk/technology/about-li-ion-batteries/
3. *Lithium-Ion Batteries: Science and Technologies*; Yoshio, M.;Brodd, R. J.; Kozawa, A., Ed; Springer Science Bussiness Media, LLC **2009**
4. Akira, A. "Secondary Battery", U.S. Pattent, 1985, US4668595
5. Scrosati, B. *Electrochimi. Acta,* **2000**, 45, 2461-2466
6. Kim. T.-H; Park, J.-S.; Chang, S. K.; Choi, S.; Ryu, J. H; Song, H.-K. *Adv. Energy. Mater.,* **2012**, 2, 860-872
7. Whittingham, M. S. *Chem. Rev.,* **2004**, 104, 4271-4301
8. Dudney, N. *J. Electrochem. Soc. Interface*, **2008**, 44-48
9. West, W. C.; Whitacre, J. F.; White, V.; Ratnakumar, B. V. *J. Micromech. Microeng.,* **2002**, 12, 58
10. Dudney, N. J. *Mat. Sci. Eng. B,* **2005**, 116, 245-247
11. Bates, J. B.; Dudney, N. J.; Neudecker, B. J.; Hart, F. X.; Jun, H. P.; Hackney, S. A.; *J. Electrochem. Soc.*, **2009**, 147, 59-64
12. Hayashi, M; Takahashi, M; Sakurai, Y. *J. Power Sources,* **2007**, 174, 990
13. Bates, J. B.; Dudney, N. J.; Gruzalski, G. R.; Zuhr, R. A.; Choudhury, A.; Luck, C. F.; Robertson, J, D. *Solid State Ionics,* **1992**, 53-56, 647-660
14. Neudecker, B. J.; Dudney, N. J; Bates, J. B. *J. Electrochem. Soc.,* **2000**, 147, 517-522

15. Padhi, K; Nanjundaswamy, K. S.; Goodenough, J. B. *J. Electrochem. Soc.*, **1997**, 114, 1188-1191

16. Zhang, W.-J. *J. Power Sources,* **2011**, 196, 13-24

17. Chiu, K.-F. *J. Electrochem. Soc.*, **2007**, 154, 129-133

18. Chiu, K.-F, Tang, H.-Y, Lin, B.-S. *J. Electrochem. So.*, **2007**, 154, 364-368

19. Zhu, X.-J.; Cheng, L-B.; Wang, C.-G.; Guo, Z.-P.; Zhang, P.; Du, G.-D.; Liu, H.-K. *J. Phys. Chem. C*, **2009**, 113, 14518–14522

20. Iriyama, Y.; Yokoyama, M.; Yada, C,; Jeong, S.-K; Yamada, I.; Abe, T.; Inaba, M.; Ogumia. Z. *Electrochemi. Solid-State Lett.*, **2004**, 7, A340-A342

21. Yada, C.; Iriyama, Y.; Jeong, S.-K.; Abe, K.; Inab, A.; Ogumi, Z. *J. Power Sources*, **2005**, 146, 559-564

22. Eftekhari . A. *J. Power Sources*, **2004**, 130, 260-265

23. Eftekhari. A. *J. Electrochem. Soc.*, **2004**, 151, A1816-A1819

24. Lu, Z. G.; Cheng, H.; Lo, M. F.; Chung, C. Y, *Adv. Funct. Mater.*, **2001**, 17, 3885-3896

25. Lu, Z. G.; Lo, M. F.; Chung, C. Y. *J. Phys. Chem. C*, **2008**, 112, 7069-7078

26. Nam, S.-H.; Kim, K.-S.; Shim, H.-S.; Lee, S. H.; Jung, Y.; Kim, W. B. *Nano Lett.*, **2011**, 11, 3656–3662

27. Hassoun, J.; Panero, S.; Simon, P.; Taberna, P. L.; Scrosati, B. *Adv. Mater.*, **2007**, 19, 1632-1635

28. Cheah, S. K.; Perre, E.; Rooth, M.; Fondell, M.; Hårsta, A.; Nyholm, L.; Boman, M.; Gustafsson, T.; Lu, J.; Simon, P.; Edström, K. *Nano Lett.*, **2009**, 9, 3230-3235

29. Shaijumon, M. M.; Perre, E; Daffos, B.; Taberna, P. L.; Tarascon, J. -M.; Simon, P. *Adv. Mater.*, **2010**, 22, 4978-4983

30. Molchan, I. S.; Molchan, T. V.; Gaponenko, N. V.; Skeldon, P.; Thompson, G. E. *Electrochem. Commun.*, **2010**, 12, 693-701

31. Chen, X.; Gerasopoulos, K.; Guo, J.; Brown, A.; Wang, C. *ACS Nano*, **2010**, 4, 366-372

32. Royston, E.; Ghosh, A.; Kofinas, P.; Harris, M. T.; Culver, J. N. *Langmuir*, **2008**, 24, 906-912

33. Dujardin, E.; Peet, C.; Stubbs, G.; Culver, J. N.; Mann, S. *Nano Lett.*, **2003**, 3, 413-417

34. Phan, V. P.; Pecquenard, B.; Cras, F. L. *Adv. Funct. Mater.*, **2012**, 22, 2580-2584

35. Long, J. W; Dunn, B.; Rolison, D. R.; White, H. S. *Chem. Rev.*, **2004**, 104, 4463-4492

36. Sides, C. R.; Croce, F.; Young, V. Y.; Martin, C. R.; Scrosati, B. *Electrochem. Solid-State Lett.*, **2005**, 8, A484-A487

37. Qu, J.; Li, H.; Henry, J. J.; Martha, S. K.; Dudney, N. J.; Xu, H.; Chi, M.; Lance, M. J.; Mahurin, S. M.; Besmann, T. M.; Dai, S. *J. Power Sources*, **2012**, 198, 312-317

38. Gowd, S. R.; Reddy, A. L. M.; Zhan, X.; Jafry, H. R.; Ajayan, P. M. *Nano Lett.*, **2012**, 12, 1198-1202

39. Lee, Y. J.; Yi, H.; Kim, W.; Kang, K.; Yun, D. S.; Strano, M. S.; Ceder, G.; Belcher, A. M. *Science*, **2009**, 324, 1051-1055

40. Lee, Y. J.; Belcher, A. M; J. *Mater. Chem.*, **2011**, 21, 1033–1039.

41. Hong, J.; Wang, C.; Dudney, N. J.; Lance, M. J. *J. Electrochem. Soc.*, **2007**, 154, A805-A809

42. Wang, W.; Tian, M.; Abdulagatov, A.; George,S. M.; Lee,; R. Yang, Y. C. *Nano Lett.*, **2012**, 12, 655-660

43. Kim, C.; Park, S.; Cho, J.; Lee, D.; Park, T.; Lee, W.; *J. Raman Spectrosc.*, **2004**, 35, 928-933

44. Kim, C.; Jeong, Y. I.; Ngoc, B. T. N.; Yang, K. S.; Kojima, M.; Kim, Y. A. *Small*, **2007**, 3, 91-95

45. McCann, J. T.; Lim, B.; Ostermann, R.; Rycenga, M.; Marquez, M.; Xia, Y. *Nano Lett.*, **2007**, 7, 2470-2474

46. Tang, M.; Carter, W. C.; Chiang, Y. -M. *Annu. Rev. Mater. Res.*, **2010**, 40, 501-529

47. Pei, B.; Wang, Q.; Zhang, W.; Yang, Z.; Chen, M. *Electrochim. Acta*, **2011**, 56, 5667-5672

48. Rui, X. H.; Jin, Y.; Feng, X. Y.; Zhang, L. C.; Chen, C. H.; *J. Power Sources*, **2011**, 196, 2109-2114

49. Hosono, E.; Wang, Y.; Kida, N.; Enomoto, M.; Kojima, N.; Okubo, M.; Matsuda, H.; Saito, Y.; Kudo, T.; Honma, I.; Zhou, H. *ACS Appl. Mater. Interfaces*, **2010**, 1, 212-218

50. Min, G. G.; Ko, Y.; Kim, T.-H.; Song, H. -K.; Kim, S. B.; Park, S. M.; *J. Electrochem. Soc.*, **2011**,158, A1267-A1274

51. Atebamba, J.-M.; Moskon, J.; Pejovnik, S.; Gabersceka, M. *J. Electrochem. Soc.*, **2010**, 157, A1218-A1228

52. Gaberscek, M.; Dominko, R.; Jamnik, J. *J. Power Sources*, **2007**, 174, 944–948

53. Zhu, X. J. ; Cheng, L.B. ; Wang, C. G. ; Guo, Z. P. ; Zhang, P.; Du, G. D.; Liu, H. K. *J. Phys. Chem. C*, **2009**, 113, 14518–14522

54. Song, S.-W.; Reade, R. P. ; Kostecki, R.; Striebel, K. A. *J. Electrochem. Soc.*, **2006**, 153. A12-A19

55. Palomares, V.; Serras, P.; Villaluenga, I.; Hueso, K. B.; Carretero-Gonzalez, J.; Rojo, T. *Energy Environ. Sci.*, **2012**, 5, 5884-5901

56. Ong, S. P.; Chevrier, V. L.; Hautier, G.; Jain, A.; Moore, C.; Kim, S.; Ma, X.; Ceder, G. *Energy Environ. Sci.*, **2011**, 4, 3680-3681

57. Kim, S. -W.; Seo, D. -H.; Kim, H.; Park. K. -Y.; Kang. K. *Phys. Chem. Chem. Phys.*, **2012**, 14, 3299-3303

58. Kim, D.; Lee, E.; Slater, M.; Lu, W.; Rood, S.; Johnson, C. S. *Electrochem. Commun.*, **2012**, 18, 66-69

59. Ellis, B. L.; Makahnouk, W. R. M.; Makimura, Y.; Toghill, K.; Nazar, L. F. *Nat. Mater.*, **2007**, 6, 749-753

60. Jian, Z.; Zhao, L.; Pan. H.; Hu.Y. -S.; Li, H.; Chen, W.; Chen, L. *Electrochem. Commun.*, **2012**, 14, 86-89

61. Cao, Y.; Xiao, L.; Wang, W.; Choi, D.; Nie, Z.; Yu, J.; Saraf, L. V.; Yang, Z.; Liu, J. *Adv. Mater.*, **2011**, 23, 3155-3160

62. D'Arienzo, M.; Ruffo, R.; Scotti, R.; Morazzoni, F.; Mari, C. M.; Polizzib, S. *Phys. Chem. Chem. Phys.*, **2012**, 14, 5945-5952

63. Kitajoua, A.; Komatsub, H.; Chiharac, K.; Gochevac, I. D.; Okadac, S.; Yamaki, J. *J. Power Sources*, **2012**, 198, 389-392

64. Lee, K. T.; Ramesh, T. N.; Nan, F.; Botton, G.; Nazar. L. F. *Chem. Mater.*, **2011**, 23, 3593-3600

65. Reynauda, M.; Barpandaa, P.; Roussec, G.; Chotarda, J.; Melota, B. C.; Rechama, N.; Tarascon, J. -M. *Solid State Sciences*, **2012**, 14, 15-20

66. Sathiya, M.; Hemalatha, K.; Ramesha, K.; Tarascon, J. -M.; Prakash, A. S. *Chem. Mater.*, **2012**, 24, 1846-1853

67. Yabuuchi, N.; Kajiyama, M.; Iwatate, J.; Nishikawa, H.; Hitomi, S.; Okuyama, R.; Usui, R.; Yamada. Y.; Komaba, S. *Nat. Mater.*, **2012**, 11, 512-517

68. Hamani, D.; Ati, M.; Tarascon, J. -M.; Rozier, P. *Electrochem. Commun.*, **2011**, 13, 938-941

69. Wessells, C. D.; Peddada, S. V.; Huggins, R. A.; Cui, Y. Nickel *Nano Lett.*, **2011**, 11, 5421-5425

70. Lu, Y.; Wang, L.; Cheng, J.; Goodenough, J. B. *Chem. Commun.*, **2012**, 48, 6544-6546

71. Abouimrane, A.; Dambournet, D.; Chapman, K. W.; Chupas, P. J.; Weng, W.; Amine, K. *J. Am. Chem. Soc.*, **2012**, 134, 4505-4508

72. Tepavcevic, S.; Xiong, H.; Stamenkovic, V. R.; Zuo, X.; Balasubramanian, M.; Prakapenka, V. B; Johnson, C. S.; Rajh, T. *ACS Nano*, **2012**, 6,530-538

73. Alcantara. R.; Jimenez-Mateos, J. M.; Lavela, P.; Tirado, J. L. *Electrochem.Commun.*, **2001**, 3, 639-642

74. Komaba, S.; Murata, W.; Ishikawa, T.; Yabuuchi, N.; Ozeki, T.; Nakayama, T.; Ogata, A.; Gotoh, K.; Fujiwara, K. *Adv. Funct. Mater.*, 2011, 21, 3859–3867

75. Wenzel, S.; Hara, T.; Janek, J.; Adelhelm. P. *Energy Environ. Sci.*, **2011**, 4, 3342

76. Komaba, S.; Ishikawa, T.; Yabuuchi, N.; Murata, W.; Ito, A.; Ohsawa, Y. *ACS Appl. Mater. Interfaces*, **2011**, 3, 4165-4168

77. Cao, Y.; Xiao, L.; Sushko, M. L.; Wang, W.; Schwenzer, B.; Xiao, J.; Nie, Z.; Saraf, L. V.; Yang, Z.; Liu, J. *Nano Lett*. **2012**, 12, 3783-3787

78. Xiong, H.; Slater, M. D.; Balasubramanian, M.; Johnson, C. S.; Rajh, T. *J. Phys. Chem. Lett.*, **2011**, 2, 2560-2565

79. Sun, Q.; Ren, Q.; Li, H.; Fu, Z. *Electrochem. Commun.*, **2011**, 13, 1462-1464.

80. Qian, J.; Chen, Y.; Wu, L.; Cao, Y.; Ai, X.; Yang. H. *Chem. Commun.*, **2012**, 48, 7070-7072

81. Xiao, L.; Cao, Y.; Xiao, J.; Wang, W.; Kovarik, L.; Nie, Z.; Liu, J. *Chem. Commun.*, **2012**, 48, 3321-3323

82. Komaba, S.; Matsuura, Y.; Ishikawa, T.; Yabuuchi, N.; Murata, W.; Kuze, S. *Electrochem. Commun.*, **2012**, 21, 65-6

83. Chevrier, V. L.; Ceder, G. *J. Electrochem. Soc.*, **2011**, 158, A1011-A1014

84. Xu, Y.; Zhu, Y.; Liu, Y.; Wang, C. *Adv. Energy Mater.*, **2013**, 3, 128-133

85. Winter, M.; Besenhard, J. O. *Electrochimi. Acta*, **1999**, 45, 31-50

86. Liu, Y.; Zhang, W.; Zhu, Y.; Luo, Y.; Xu, Y.; Brown, A.; Culver, J. N.; Lundgren, C. A.; Xu, K.; Wang, Y.; *et al. Nano Lett.*, **2013**, 13, 293-300

87. Cui, L. -F.; Ruffo, R.; Chan, C. K.; Peng, H.; Cui, Y. *Nano Lett.*, 2009, 9, 491-495

88. Bruce, P. G.; Scrosati, B.; Tarascon, J. -M. *Angew. Chem. Int. Ed.*, **2008**, 47, 2930-2946

89. Mukaiboa, H.; Mommaa, T.; Osaka, T. *J. Power Sources*, **2005**, 146, 457-463

90. Nishikawa, K.; Fukunaka, Y.; Sakka, T.; Ogata, Y.; Selman, J. R. *J. Power Sources*, **2007**, 174, 668-672

91. Guo, H.; Zhao, H.; Jia, X. *Electrochem. Commun.*, **2007**, 9, 2207-2211

92. Ehinon, K. K. D.; Naille, S.; Dedryve`re, R.; Lippens, P. -E.; Jumas, J. -C.; Gonbeau, D. *Chem. Mater.*, **2008**, 20, 5388-5398

93. Nishikawa, K.; Dokkob, K.; Kinoshita, K.; Woo, S. -W.; Kanamura, K. *J. Power Sources*, **2009**, 189, 726-729

94. Huang, L.; Wei, H. -B.; Ke, F. -S.; Fan, X. -Y.; Li, J. -T.; Sun, S. -G. *Electrochim. Acta*, **2009**, 54, 2693-2698

95. Woo, S. -W.; Okada, N.; Kotobuki, M.; Sasajima, K.; Munakata, H.; Kajihara, K.; Kanamura, K. *Electrochim. Acta*, **2010**, 55, 8030-8035

96. Noh, M.; Kwon, Y.; Lee, H.; Cho, J.; Kim, Y.; Kim, M. G. *Chem. Mater.*, **2005**, 17, 1926-1929

97. Yu, Y.; Gu, L.; Wang, C.; Dhanabalan, A.; Aken, P. A. V.; Maier. J. *Angew. Chem. Int. Ed.*, **2009**, 48, 6485-6489

98. Derrien, G.; Hassoun, J.; Panero, S.; Scrosati, B. *Adv. Mater.*, **2007**, 19, 2336-2340

99. Fan. J.; Wang, T.; Yu, C.; Tu, B.; Jiang, Z.; Zhao, D. *Adv. Mater.*, **2004**, 16, 1432-1436

100. Lee, K. T.; Jung, Y. S.; Oh, S. M. *J. Am. Chem. Soc.*, **2003**, 125, 5652-5653

Publication and Presentation

Publication

Publications that have appeared in print

1. **Y. Liu**, Y. Xu, Y. Zhu, J. Culver, C. Lundgren, K. Xu, C. Wang, "Tin Coated Viral-Nanoforests as Sodium-Ion Battery Anodes" *ACS Nano*, **2013**, 7, 3627

2. Y Xu, Y. Zhu, **Y. Liu**, and C. Wang, "Electrochemical Performance of Porous Carbon/Tin Composite Anodes for Sodium-Ion and Lithium-Ion Batteries" *Advanced Energy Materials*, **2013**, 3, 128

3. A. Langrock; Y. Xu, **Y. Liu**; S. Ehrman, A. Manivannan, C. Wang, "Carbon Coated Hollow Na_2FePO_4F Spheres for Na-ion Battery Cathodes" *Journal of Power Sources*, **2013**, 223, 62

4. Y. Zhu, Y. Xu, **Y. Liu**, C. Luo and C. Wang, "Comparison of Electrochemical Performances of Olivine $NaFePO_4$ in Sodium-Ion Batteries and Olivine $LiFePO_4$ in Lithium-Ion Batteries" *Nanoscale*, **2013**, 5, 780

5. Y. Xu, Q. Liu, Y. Zhu, **Y. Liu**, A. Langrock, M. R. Zachariah, and C. Wang, "Uniform Nano-Sn/C Composite Anodes for Lithium Ion Batteries" *Nano Letters*, **2013**, 13, 470

6. **Y. Liu**, W. Zhang, Y. Zhu, Y. Luo, Y. Xu, A. Brown, J. N. Culver, C.A. Lundgren, K. Xu, Y. Wang, and C. Wang, "Architecturing Hierarchical Function Layers on Self-Assembled Viral Templates as 3D Nano-Array Electrodes for Integrated Li-Ion Microbatteries" *Nano Letters*, **2013**, 13, 293

7. Y. Luo, J. Guo, **Y. Liu**, Q. Shao, C. Wang, and D. Chu, "Copolymerization of Methyl Methacrylate and Vinylbenzyl Chloride towards Alkaline Anion Exchange Membrane for Fuel Cell Applications" *Journal of Membrane Science*, **2012**, 209, 432

Publications that have been submitted and are under review

1. **Y. Liu**, Y. Xu, Y. Zhu, C. Lundgren, K. Xu, C. Wang, " Uniform LiF/Co/C Nanocomposite as Anode Material for Lithium Ion Batteries", submitted, April 04, 2013
2. Y. Xu, G. Jian, **Y. Liu**, Y. Zhu, M. Zachariah, C, Wang, "Mesoporous Fe2O3 Anodes for Lithium-Ion Batteries", submitted, May 04, 2013

Presentation

Presentations that have been delivered

Y. Liu, "Virus Enabled 3D Nano-Array Electrodes for Integrated Li/Na-Ion Microbatteries", Dean's Annual Research Competition, College Park, Maryland, April 28, 2013.